



David José Pintão dos Santos Fontes Barbosa

Licenciado em Ciências da Engenharia Mecânica

**Gas Tungsten Arc Welding
of
NiTi Shape Memory Alloy**

Dissertação para obtenção do Grau de Mestre em
Engenharia Mecânica

Orientador: Doutora Rosa Maria Mendes Miranda,
Professora Associada com Agregação, Faculdade de
Ciências e Tecnologia da Universidade Nova de Lisboa

Co-orientador: Mestre João Pedro de Sousa Oliveira,
Faculdade de Ciências e Tecnologia da Universidade
Nova de Lisboa

Júri:

Presidente: Prof. Doutor Jorge Joaquim Pamies Teixeira
Vogais: Prof. Doutora Maria Luísa Coutinho Gomes de Almeida
Prof. Doutor Francisco Manuel Braz Fernandes
Prof. Doutora Rosa Maria Mendes Miranda

Gas Tungsten Arc Welding of Shape Memory Alloy NiTi

Copyright © 2014 David José Pintão dos Santos Fontes Barbosa

Faculdade Ciências e Tecnologia, Universidade Nova de Lisboa

A Faculdade de Ciências e Tecnologia e a Universidade Nova de Lisboa tem o direito, perpétuo e sem limites geográficos, de arquivar e publicar esta dissertação através de exemplares impressos reproduzidos em papel ou de forma digital, ou por qualquer outro meio conhecido ou que venha a ser inventado, e de a divulgar através de repositórios científicos e de admitir a sua cópia e distribuição com objetivos educacionais ou de investigação, não comerciais, desde que seja dado crédito ao autor e editor.

AGRADECIMENTOS

Gostaria de expressar a minha gratidão a todos aqueles que me acompanharam ao longo deste período e aos que, direta ou indiretamente, estiveram envolvidos nesta investigação e sem os quais teria sido impossível torná-la realidade.

À minha orientadora, professora Rosa Miranda, primeiro pelo amável convite para este projeto, depois pela dedicação, disponibilidade, empenho e tempo despendido, consubstanciados no apoio que me foi dando ao longo da realização desta investigação. De salientar que foi também um prazer conviver, com a professora, nesta fase da minha vida académica, com quem aprendi muito, sendo de realçar que pertence ao grupo de docentes que mais me marcou ao longo do curso.

Ao meu co-orientador, Mestre João Oliveira que foi crucial, na fase inicial, para o arranque do trabalho orientando-me e, numa fase posterior, mostrou-se sempre disponível e interessado, mesmo à distância, ao arranjar tempo para me auxiliar no que quer que fosse necessário.

Ao professor Braz Fernandes, pelo interesse e pela disponibilizada que sempre demonstrou para me auxiliar ao longo do desenvolvimento desta investigação. Ao professor Rui Silva pela ajuda prestada na realização dos ensaios de SEM/EDS. Também gostaria de agradecer ao Pablo Vigarinho, pelo apoio que me deu aquando da realização de ensaios no CENIMAT.

Aos Srs. António Campos e Paulo Magalhães, com quem tive o prazer de conviver grande parte do período de implementação da fase experimental, pelo grande apoio e pela amizade demonstrada.

Aos professores Pâmies Teixeira e Telmo Santos, pela cedência de “hardware”, sem o qual não poderia realizar a experimentação da investigação, como também pelo apoio que me foram dando ao longo da mesma. De salientar também que, a par da professora Rosa, pertencem ao grupo de docentes com quem tive o prazer e privilégio de aprender e os quais considero exemplos a seguir.

À Omnidea, pela cedência da máquina de soldadura TIG, imprescindível para o desenvolvimento desta tese.

Aos meus colegas do laboratório de END, com quem privei alguns momentos, pela ajuda imprescindível na colocação do braço mecânico a funcionar, como também ao Renato Guerreiro e António Soares pela cedência das suas impressoras 3D para produzir as peças do "trigger". Referir a A. J. MALTEZ - SOCIEDADE METALÚRGICA, LDA, pela disponibilidade e alteração do aparelho para avaliação do efeito de memória de forma.

Aos meus colegas de turma - "Geração 09" - porque me acompanharam ao longo de todo o percurso académico e aos que entretanto chegaram nos anos seguintes, afilhados e caloiros e que de certa forma me marcaram e em parte me ajudaram a definir quem sou. Os importantes sabem quem são.

Aos meus grandes amigos do NAve- Associação Nova Aventura, com quem vivi grandes momentos e aventuras e que desde cedo estiveram presentes dando sempre apoio.

Às famílias Lamelas, Souto, Leiria, Paradela e Corte-Real por me terem acolhido e feito sentir como da casa e por todo o apoio que me foram dando ao longo deste período.

Às 3 gerações do grupo "Parolos", por serem simplesmente quem são. De realçar a minha madrinha, Conceição Ferreira, por estar sempre presente.

À Ana Rodrigo, pela amizade que sempre demonstrou como também por todo o apoio dado nesta fase final.

Ao Alexandre Manuel Costa, por toda a amizade demonstrada e por todos estes anos de convivência, sem dúvida um amigo para a vida. À sua família também, pela forma hospitaleira e amiga como sempre me recebeu.

Aos meus amigos de sempre, os meus irmãos Ivo Carrilho e Rudy Ribeiras e às suas famílias, que sempre estiveram e que sei que continuarão sempre presentes.

À Titi, à Irene e aos meus primos Clotilde e António pelo carinho, atenção e dedicação que demonstram e por garantirem que está sempre tudo bem.

Aos meus tios e primos, por terem estado sempre presentes e por me fazerem sentir em casa.

À minha mãe Guida, ao meu pai Simão e ao meu irmão Hugo, que me deram a estabilidade, apoio e força necessários ao longo deste período, permitindo-me assim terminá-lo. Obrigado por fazerem parte da minha vida. Se sou o que sou hoje, é graças a vocês.

ACKNOWLEDGEMENTS

I'd like to express my gratitude to all those who accompanied me during the time I was doing this project and to whom, direct or indirectly, were involved on this investigation and without them I was unable to come this true.

To my assigned advisor, teacher Rosa Miranda, first of all by her kind invitation to perform this project, afterwards by her dedication, time and commitment, embodied on the support she gave to me during this investigation. It should be noted that was also my pleasure to spend time with my assigned advisor on this stage of my academic life, with whom I learned too much, being one of the teachers who I will never forget.

To my assistant advisor, Master João Oliveira who was crucial at beginning of my thesis, guiding me and afterwards, even from far away, being always available and interested to help me in what was needed.

To professor Braz Fernandes, by his concern and availability always showed to help me during my investigation. To professor Rui Silva for the help given during SEM/EDS measurements. Also to thank Paulo Vigarinho for his support with the test procedures at CENIMAT.

To Mr. António Campos and Mr. Paulo Magalhães, which whom I had the pleasure to be with during large period of the experimental phase of implementation of this project, by their support and friendship.

To my teachers Pamies Teixeira and Telmo Santos, who provide me the necessary hardware to perform my investigation, as for their support during the investigation. To be noted that, in line with teacher Rosa, they belong to the group of teachers that was my pleasure and privilege to have learned and I consider examples to follow.

To Omnidea, for lending me TIG welding machine, essential to develop this thesis.

To my colleagues of END Laboratory, with whom I private for a while, for their unforgettable help to put the mechanical arm working, and Renato Guerreiro and António Soares also for lending me their 3D printers to produce the pieces of the "trigger". Mention to *A. J. MALTEZ - SOCIEDADE METALÚRGICA, LDA* for their availability to machine the device to evaluate the shape memory effect.

To my classmates - "Class of 2009" – as we stood side by side during our academic journey and those who arrived during followed years, referrals and freshmen's that on a certain way marked and partially allowed me to define who I am. The key colleagues know who they are.

To my good friends of Nave – Associação Nova Aventura, with whom I lived big moments and adventures and earlier were present with their support.

To Lamelas, Souto, Leiria, Paradela and Corte-Real families, because of their strong support that given during this period and allowing me to became part of their family.

To the 3 generation of "Parolos" Group, as they are just as they are. Highlighting my Godmother, Conceição Ferreira, for allways being present.

To Ana Rodrigo, for her friendship always showed as for her support during this final stage.

To Alexandre Manuel Costa, for all his friendship and for all those years of conviviality. With no doubt a friend for life. Also to his family, by their hospitality and friendly welcome they received me at their home.

To my forever friends/brothers Ivo Carrilho and Rudy Ribeiras and their families, always present and as I know they will keep their presence.

To Titi, to Irene and to my cousins Clotilde and António for their affection, attention and for making sure that everything was always all right.

To my uncles, aunts and cousins, for always being present and for making me feel at home.

To my mother Guida, father Simão and my brother Hugo, by their support, stability and strength, given during this period, that allow me to finish my thesis. Many thanks for being part of my life. If I am who I am, is due to you.

Mamani, Bhava! Kanimambo!

(Mãe, Pai! Obrigado!)

ABSTRACT

Shape memory alloys are characterized by the ability of recovering their initial shape after being deformed and by superelasticity. Since the discovery of these alloys, a new field of interest emerged not only for the scientific community but also to many industries. However, these alloys present poor machinability which constitute a constrain in the design of complex components for new applications. Thus, the demand for joining techniques able to join these alloys without compromising their properties became of great importance to enlarge the complexity of existing applications. Literature shows that these alloys are joined mainly using laser welding.

In the present study, similar NiTi butt joints, were produced using TIG welding. The welds were performed in 1.5 mm thick plates across the rolling direction. A special fixture and gas assist device was designed and manufactured. Also a robot arm was adapted to accommodate the welding torch to assure the repeatability of the welding parameters. Welds were successfully achieved without macroscopic defects, such as pores and distortions. Very superficial oxidation was seen on the top surface due to insufficient shielding gas flow on the weld face. The welded joints were mechanically tested and structurally characterized. Testing methods were used to evaluate macro and microstructure, as well as the phase transformation temperatures, the mechanical single and cyclic behaviour and the shape recovery ability. Differential Scanning Calorimetry (DSC), Scanning Electron Microscopy (SEM), Energy Dispersive Spectroscopy (EDS), microhardness measurements were techniques also used to evaluate the welded joints.

A depletion in Ni in the fusion zone was seen, as well as a shift in M_s temperature. For strain values of 4% the accumulated irrecoverable strain was of about 30% and increased with the strain imposed during cycling. Nevertheless, a complete recovery of initial shape was observed when testing the shape memory effect on a dedicated device that introduces a deformation of 6.7%. That is, the welding procedure does not remove the ability of the specimens to recover their initial shape.

KEY-WORDS

Shape Memory Alloys

NiTi

Welding

TIG

Shape Memory Effect

Superelasticity

RESUMO

As ligas com memória de forma são ligas metálicas caracterizadas pela capacidade de recuperar a forma mesmo depois de serem deformadas e pela superelasticidade. Desde a sua descoberta este tipo de liga despertou o interesse da comunidade científica e de várias indústrias. Contudo, estas ligas são de difícil processamento, sendo um impedimento ao desenvolvimento e de novas aplicações requerendo formas mais complexas. Assim, tem-se investigado técnicas de ligação capazes de unir estas ligas sem comprometer as suas propriedades. Na literatura, estas ligas são unidas maioritariamente por soldadura laser.

No presente trabalho, foram produzidas juntas similares topo a topo de chapas de NiTi, utilizando o processo de soldadura TIG - Tungsten Inert Gas. As juntas foram feitas perpendicularmente à direção de laminagem e utilizaram-se chapas com 1,5 mm de espessura. Foi desenvolvido um sistema de fixação e de proteção gasosa para produzir as juntas soldadas e adaptado um braço mecânico para acomodar a tocha de soldadura por forma a garantir a repetibilidade do processo. Posteriormente, as juntas soldadas foram testadas mecanicamente através de testes de tração uniaxial, ciclagens e estudos do efeito de memória de forma; e caracterizadas estruturalmente com técnicas de análise como: a Microscopia Eletrónica de Varrimento (SEM), Energy Dispersive Spectroscopy (EDS), Microdurezas, Calorimetria Diferencial de Varrimento (DSC) e Difração de Raios-X (DRX).

Verificou-se uma diminuição da percentagem atómica de Ni na zona fundida bem como uma alteração da temperatura M_s . Para valores de deformação de 4% a deformação acumulada não recuperável foi de cerca de 30% e aumentava com a % de deformação imposta durante a ciclagem. Não obstante, verificou-se uma recuperação completa da forma inicial dos provetes quando testados ao efeito de memória de forma num dispositivo dedicado que introduz uma deformação de 6.7%. Isto é, a soldadura não retira a capacidade de recuperação total da forma inicial.

PALAVRAS-CHAVE

Ligas com memória de forma

NiTi

Soldadura TIG

Efeito de Memória de Forma

Superelasticidade

CONTENTS

AGRADECIMENTOS	v
Acknowledgements	vii
ABSTRACT	xi
KEY-WORDS	xii
RESUMO	xiii
PALAVRAS-CHAVE.....	xiv
LIST OF FIGURES.....	xix
LIST OF TABLES.....	xxi
1 - INTRODUCTION	1
1.1 - Motivation	1
1.2 - Objectives	2
1.3 - Thesis structure	2
2 - WELDING SHAPE MEMORY ALLOYS	3
2.1 - Shape Memory Alloys - SMAs.....	3
2.2 - Characterization of SMAs.....	4
2.3 - Welding processes of Shape Memory Alloys	11
2.3.1 - Gas Tungsten Arc Welding - GTAW.....	11
2.3.2 - Laser Welding.....	14
2.4 - NiTi Similar Joints	15
2.5 - Applications	16
2.5.1 - Aerospace Applications	17
2.5.2 - Medical Applications	19
2.5.3 - Transportation Applications.....	21
2.5.4 - Other Applications.....	21
2.6 Summary.....	22
3 - Equipment Developed	23

3.1 - Positioning Device	23
3.2 - Trigger Device.....	25
3.3 - Adapted Equipment	25
3.3.1 Moving Table	25
3.3.1.1 Testing Device For Shape Memory Effect Evaluation ...	26
4 - Experimental Procedure.....	29
4.1 - Materials.....	30
4.2 - Welding Equipment.....	31
4.3 - Experimental Approach.....	32
4.3.1 - Butt joints.....	32
Samples Preparation For Testing.....	32
4.3.2 - Testing Methods.....	33
- Microstructure Observations	33
- Differential Scanning Calorimetry - DSC	34
- X-Ray Diffraction Analysis - XDR.....	34
- Microhardness Measurements	34
- Mechanical Tests	34
Uniaxial Tensile Testing.....	34
Cycling Tests	35
- Shape Memory Effect - SME.....	35
5 - Results and discussion	37
5.1 - Macroscopic observations.....	38
5.2 - Micro Observations	39
5.2.1 Microscope Observations.....	39
5.2.2 Scanning Electron Microscopy - SEM/EDS	40
5.3 - Differential Scanning Calorimetry measurements - DSC	41
5.4 - Microhardness Measurements	43
5.5 - X-ray Diffraction Analysis.....	44

5.6 - Mechanical Tests	45
5.6.1 - Tensile Tests	45
5.6.2 - Cycling Behavior.....	46
- Cycling Tests.....	46
- Accumulated Irrecoverable Strain.....	49
5.7 - Shape Memory Effect Evaluation.....	51
6 - Conclusions and Further Work.....	53
REFERENCES.....	57
ANNEXES	I
A - Positioning Device Technical Drawings.....	II
B - Trigger Device Technical Drawings.....	XIII

LIST OF FIGURES

Figure 2.1 - σ - ϵ diagram. (0 - 5) martensitic deformation, heat recovery until austenitic domain (SME); (5 - 10) superelastic deformation of austenite [5]	4
Figure 2.2- Cristal structure of: a) B2 austenite; b) B19 Martensite (R-phase); c) B19' Martensite [7].....	5
Figure 2.3 - Temperature-induced phase transformation of a SMA without mechanical loading [8].....	6
Figure 2.4 - Schema showing the transition from twinned to detwinned martensite at constant temperature[8].	6
Figure 2.5 - Schema of the Shape Memory Effect for a Shape Memory Alloy [8].....	7
Figure 2.6 - Temperature-induced phase transformation in the presence of applied load [8].....	8
Figure 2.7 - A superelastic loading path [8].	8
Figure 2.8 - Stress-strain curve of conventional vs. superelastic alloys [9].....	9
Figure 2.9- Representation of lattice changes in stainless steel and in a superalloy [4].	9
Figure 2.10- Ni-Ti phase diagram [10].	10
Figure 2.11- Variation of transformation temperature with Ni content for binary Ni-Ti alloys [7].....	11
Figure 2.12- Autogenous Gas Tungsten Arc Welding (GTAW) process representation (Adapted from[12]).	12
Figure 2.13- Laser welding modes: a) "keyhole" and b) Conduction [14].....	15
Figure 2.14 - Relation between heat input and the weld bead face and root width. Adapted from [1].....	16
Figure 2.15 - Variable geometry chevron [8].....	17
Figure 2.16 - SMA hinges. Folded and deployed configuration [8].....	18
Figure 2.17 - Orthodontic applications of NiTi SMA: a) NiTi braces; b) schematic of a NiTi drill used for root canal surgery [8].	19
Figure 2.18 - Cardiovascular applications: a) Simon's filter in deployed configuration; b) Self-expanding NiTi stent [8].	20
Figure 3.1- a) Top view of the base - central canal and position rulers mounted; b) perspective view of base with position rulers mounted.	24
Figure 3.2- Welding chamber.....	24
Figure 3.3 - Trigger device.....	25
Figure 3.4 - X-axis Table: a) over view of table; b) set up.....	26

Figure 3.5 - Robot arm control program interface.....	26
Figure 3.6- Device used for shape memory effect testing.....	27
Figure 3.7 - Shape Memory Effect device after modifications.....	27
Figure 4.1- TELWIN, TECHNOLOGY TIG 182 AC/DC-HF/LIFT.....	31
Figure 4.2 - Specimens extracted from welded samples.....	33
Figure 4.3 - Schema of pure bending [20].....	36
Figure 4.4 - Bending section [20].....	36
Figure 5.1 - Aspect of similar NiTi butt weld joints: a) sample #1.1; b) sample 1.2 and c) sample 1.3.....	38
Figure 5.2 - Specimen microstructure visualization.....	39
Figure 5.3 - Microstructure of: a) HAZ; b) Transition HAZ/FZ c) FZ.....	39
Figure 5.4 - EDS results from Base Material.....	40
Figure 5.5 - EDS results from Fusion Zone.....	40
Figure 5.6 - Vapour pressure as a function of temperature for Ni and Ti (Adapted from [6]).....	41
Figure 5.7 - DSC measurements of the base material and molten material for determination of the transformation temperatures.....	42
Figure 5.8 - Vickers Microhardness profiles made on specimen #1.3.2.....	43
Figure 5.9 - Microhardness measurements in the cross section of the sample along weld top and root.....	43
Figure 5.10 - XRD measurements of BM.....	44
Figure 5.11 - XRD measurements of FZ.....	44
Figure 5.12 - Tensile test performed on Base Material and specimens #1.2.3 and #1.3.4.....	45
Figure 5.13 - Cycling test up to 4% elongation.....	47
Figure 5.14 - Cycling test up to 6% elongation.....	47
Figure 5.15 - Cycling test up to 8% elongation.....	48
Figure 5.16 - Cycling test up to 12% elongation.....	48
Figure 5.17- Evolution of the accumulated irrecoverable strain for specimen cycled at 4%.....	49
Figure 5.18 - Evolution of the accumulated irrecoverable strain for specimen cycled at 6%.....	50
Figure 5.19 - Evolution of the accumulated irrecoverable strain for specimen cycled at 12%.....	50
Figure 5.20 - SME evaluation of specimen #1.2.1 - Variation of the irrecoverable angle (Ω) with time.....	51

LIST OF TABLES

Table 2.1- Characteristics of current types for Gas Tungsten Arc Welding.	13
Table 4.1- Physical properties of NiTi SMA [19].	30
Table 4.2- Mechanical properties of NiTi SMA [19].	30
Table 4.3 - TELWIN, TECHNOLOGY TIG 182 AC/DC-HF/LIFT Technical Data [20].	31
Table 4.4- Welding parameters chosen to weld the NiTi/NiTi butt joints specimens. ...	32
Table 4.5 - Specimens references and tests performed.	33
Table 4.6 - Uniaxial tensile test specimens.	35
Table 4.7 - Cycling test specimens.	35
Table 5.1 - Atomic percentage of Ti and Ni on the base material and fusion zone.	41
Table 5.2- Transformation temperatures for base material and molten material.	42
Table 5.3 - Uniaxial Tensile test results.	46
Table 5.4 - Cycling Tests results.	46
Table 5.5- Shape Memory Effect results.	51

1 - INTRODUCTION

Shape memory alloys (SMA) are known for the capacity to recover the initial shape after being deformed, when subjected to a specific thermal cycle, called Shape Memory Effect (SME). Since their discovery, in the 50's, applications using SMAs have increased significantly over the past decades and can be found in a wide variety of industrial sectors, from sensing and actuation applications, to more demanding industries as aerospace and biomedical. Although many materials can exhibit SME, just the ones that can recover the original shape are of commercial interest. Due to their properties, NiTi are amongst the most used SMAs despite their poor machinability, which limits components design. Thus, joining SMA became a field of research to overcome these limitations and enlarge further applications.

1.1 - Motivation

Previous work developed on laser welding of NiTi by Vieira [1], it was observed that the welds performed under conduction mode, that is with larger aspect ratios, exhibit better mechanical properties. So, an attempt was made in this study to weld NiTi by Tungsten Arc Welding (TIG). Though TIG has a higher heat input it has some similarities to conduction laser weld mode since there is no filler material and an inert gas is used. Additionally, TIG is less expensive than Laser welding.

1.2 - Objectives

The present study aimed at welding 1.5 mm thick NiTi plates in a butt joint configuration, using the TIG welding process and perform a structural and mechanical characterization of the joints.

For this, dedicated equipment was designed and manufactured to fix the plates. Welds were performed followed by a structural and mechanical characterization of the welded samples, using several techniques including Differential Scanning Calorimetry (DSC), Scanning Electron Microscopy (SEM), Energy Dispersive Spectroscopy (EDS), microhardness, uniaxial and cycling tensile tests and SME evaluation.

1.3 - Thesis structure

This thesis is structured in five chapters.

Chapter 1 includes a brief introduction contextualizing the study, motivation and objectives.

Chapter 2 provides the theoretical background of SMA behaviour for easier comprehension throughout the study as well as of the welding process.

Chapter 3 describes the equipment developed and the existing equipment altered.

Chapter 4 indicates the experimental procedure adopted, identifying the material used, the experimental methodology and the characterization techniques.

Chapter 5 presents and discusses the results of this investigation.

Finally, chapter 6 presents the conclusions of this study and gives suggestions for future work.

2 - WELDING SHAPE MEMORY ALLOYS

2.1 - Shape Memory Alloys - SMAs

As previously mentioned, SMA are metallic materials with the unique ability of recovering their initial shape even after being deformed. This type of alloys are characterized by the Shape Memory Effect, Superelastic Effect (SE), high damping capacity and magnetostriction. Such characteristic put SMAs in a particular class of advanced materials often called smart materials, together with other types of active materials, such as piezoelectric and magnetostrictive materials[2,3].

The functional properties of SMAs were observed during the 50's, in a Au-74.5 at % Cd alloy, the number of SMAs has continuously increased and the shape memory effect and associated properties have been identified in an increasing number of alloys, both ferrous and non-ferrous [2,3]. Several types of SMA, can be found in the market, but NiTi and Cu base alloys are the most commercialized ones and NiTi the most used since it has biocompatibility properties thus, finds use in medical applications [4]. They have higher capacity in terms of elongation recovery (8% against the 4% of Cu alloys), are more stable thermally, have better resistance to corrosion and have a wider range of transformation temperatures. NiTi alloys, are also known as "*NiTiNOL*" (commercial name) due to their composition: Nickel and Titanium in equiatomic proportions. The commercial terminology

was a tribute to the first place where they were first discovered and studied, at Naval Ordnance Laboratory (NOL), in the beginning of the year 1960. Since then, SMAs have captured the interest of the scientific community and are still the most widely studied and applied [3].

With the technological advances, many difficulties related to SMA were exceeded, but research is still needed for these alloys to reach their full potential. Despite all disadvantages regarding costs, manufacturing, processing and/or joining SMA, there has been an increased use of SMA with success in many industrial sectors such as biomedical, automotive and aeronautical.

2.2 - Characterization of SMAs

SMA are materials characterized by SME and SE, unlike conventional metals and alloys. SME is characterized by the recovery of the initial shape by heating after being deformed, while SE is characterized by strain recovery when unloading [2]. Both effects are represented in Figure 2.1.

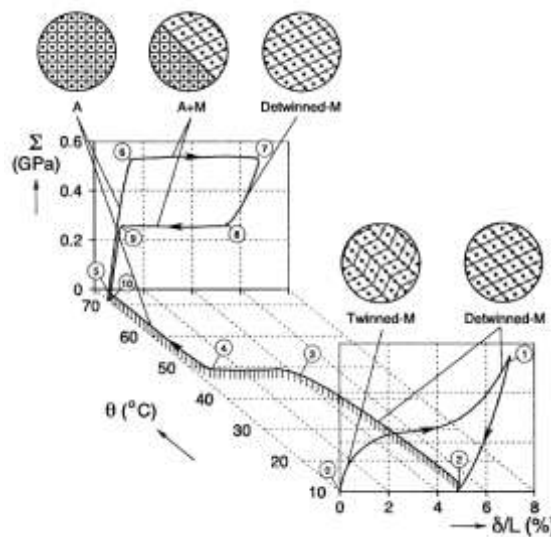


Figure 2.1 - σ - ϵ diagram. (0 - 5) martensitic deformation, heat recovery until austenitic domain (SME); (5 - 10) superelastic deformation of austenite [5].

The martensitic transformation is in the origin of the SME and SE. Unlike conventional metals, when SMAs are deformed, a significant amount of strain may be produced as a result of atomic displacements, changing the crystal structure, which is reversible. This reversible phase transformation that occurs as a result of a combination of reversible crystallographic changes (martensitic thermoelastic transformation) and/or reversible deformation processes (by twin variant reorientation), produces martensite from the austenite parent phase. The parent phase in binary NiTi system has a B2 structure, while

martensite has a monoclinic structure (B19'), the transformation from austenite to martensite can occur either in a one-step or by a two-step mode, depending on composition and thermal or thermomechanical treatments. On the two-step mode (represented in Figure 2.2), a third phase appear between austenite and martensite, called R-phase, that has a trigonal structure [3,7].

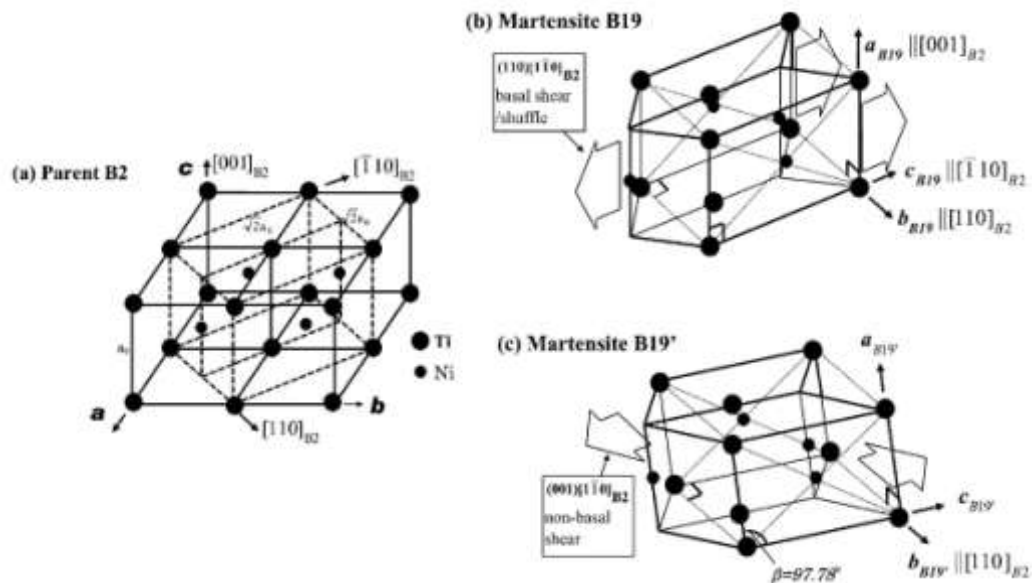


Figure 2.2- Cristal structure of: a) B2 austenite; b) B19 Martensite (R-phase); c) B19' Martensite [7].

There are two cristalgraphic forms of martensite: twinned martensite (M^t) and detwinned martensite (M^d). In the first opposite shears from opposite variants cancel, and the microscopic shape of the crystal is preserved by forming a self-accommodating structure; in detwinned martensite a particular variant is dominant and as a consequence, the shape is not preserved. Variant is the denomination given to the orientation direction of each martensite crystal formed during the martensitic transformation [1,6,8].

In the austenitic phase, upon cooling and without any stress induced, the crystal structure changes to martensite. This transition is called forward or direct transformation. It occurs due to the formation of several martensitic variants, wich can be up to 24 in NiTi, which is arranged in such way, that results in twinned martensite. If afterwards the temperature rises, the opposite transformation occurs, and martensite transforms into austenite in a reverse transformation [1,6,8].

The schematic of the crystal structure of twinned martensite and austenite for an SMA and the transformation between these are represented in Figure 2.3.

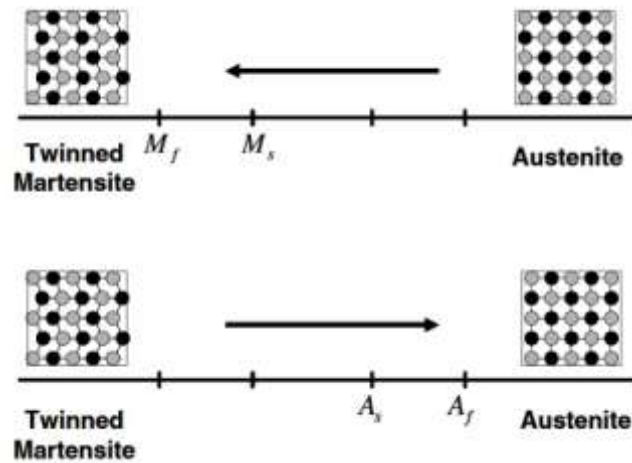


Figure 2.3 - Temperature-induced phase transformation of a SMA without mechanical loading [8].

As shown in Figure 2.3, associated with the phase transformations, there are four characteristic temperatures. During forward transformation, the austenite begins to transform to twinned martensite at the martensitic start temperature, M_s , and the transformation will be finished at martensitic finish temperature, M_f . Upon reverse transformation, there is austenitic start temperature, A_s , and austenitic finish temperature, A_f , when the transformation is fully completed.

If load is applied to the material in twinned martensite state, it is possible to obtain detwinned martensite by reorienting a certain number of variants (Figure 2.4). This detwinning process induces a macroscopic shape modification where the deformed configuration is retained when the applied load is released. A minimum amount of stress is required to start the detwinning process, called detwinning start stress (σ_s). The complete detwinning process will occur when the detwinning finish stress (σ_f) is reached [1,8].

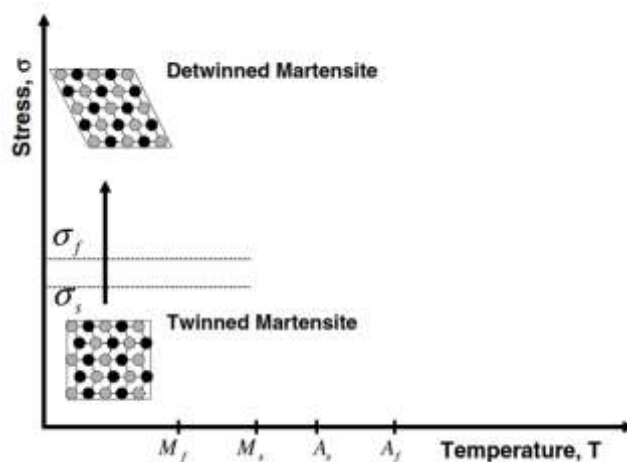


Figure 2.4 - Schema showing the transition from twinned to detwinned martensite at constant temperature[8].

SME is a such a phenomenon that, even though a sample is deformed below A_s , it regains its original shape by heating up to a temperature above A_f leading to a reverse transformation. The deformation imposed to the specimen could be of any kind such as tension, compression or bending, as long as the strain is lower than some critical value, depending on the alloy properties [2].

If a sample is cooled to a temperature below M_f , as stated before, a forward transformation occurs. However, there is no shape change since this is a self-accommodated transformation (Figure 2.3). By applying an external force, after lowering the temperature below M_f , the twin boundaries move in order to accommodate the applied force. If the stress is high enough, one single martensite variant will be favoured and there will be a modification on the shape of the specimen. When heat is applied and the temperature is higher than A_f , the reverse transformation will occur, leading to complete shape recovery [6,8]. The process described above is referred to as Shape Memory Effect and is represented in Figure 2.5.

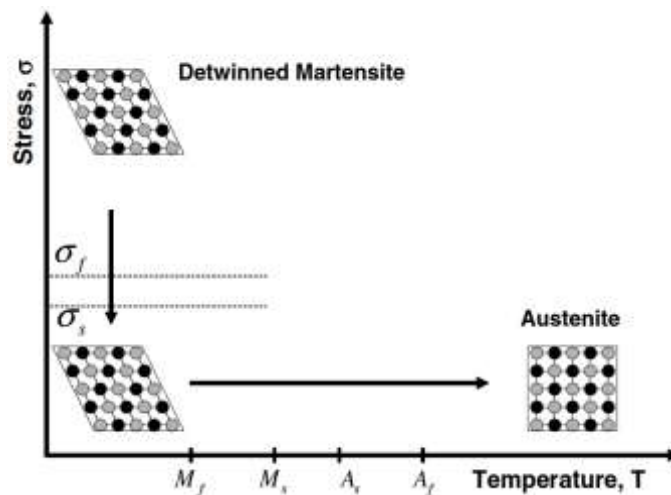


Figure 2.5 - Schema of the Shape Memory Effect for a Shape Memory Alloy [8].

Since forward and reverse transformations occur over a range of temperatures (M_s to M_f , A_s to A_f), for a given SMA composition, it is possible to build transformation regions in the stress-temperature space. The transformation temperatures are strongly dependent on the magnitude of the applied load, with higher values of applied load leading to higher transformation temperatures, as shown in Figure 2.6. Under an applied uniaxial tensile load with a corresponding stress (σ), the new transformation temperatures are represented by M_f^σ , M_s^σ , A_s^σ and A_f^σ for martensitic finish, martensitic start, austenitic start and the austenitic finish temperatures, respectively [6,8].

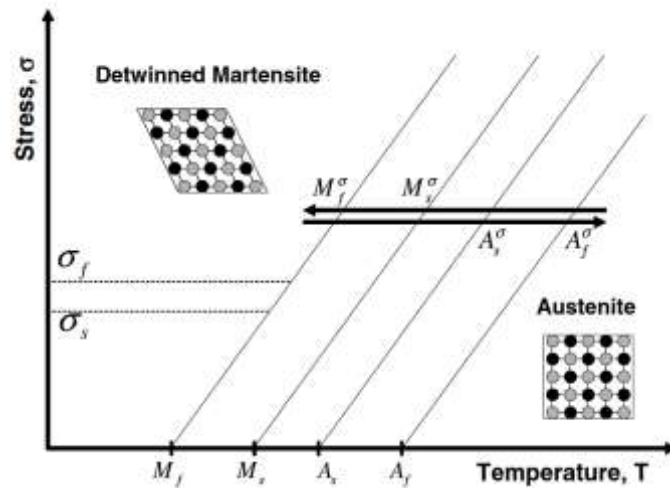


Figure 2.6 - Temperature-induced phase transformation in the presence of applied load [8].

Considering Figure 2.7, it is possible to observe that fully detwinned martensite from austenite can be attained just by applying a sufficiently high mechanical load to the material in the austenitic phase. If the temperature of the material is above A_f , a complete shape recovery is attained, just upon unloading to austenite. This material behaviour is referred as superelastic effect.

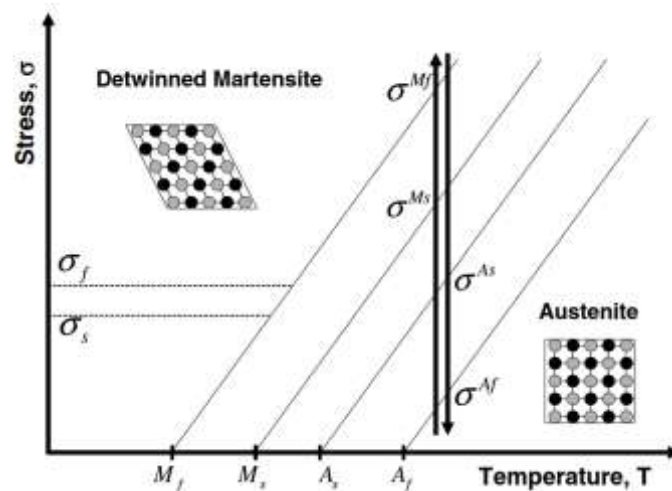


Figure 2.7 - A superelastic loading path [8].

This effect is represented in a stress-strain diagram as a hysteresis behaviour, where two plateaux can be identified (Figure 2.8). The upper one occurs during the forward transformation, while the other is seen during the reverse transformation.

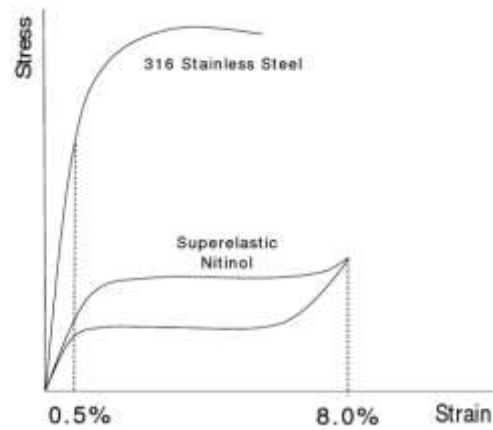


Figure 2.8 - Stress-strain curve of conventional vs. superelastic alloys [9].

Also, in figure 2.8 is possible to identify the martensitic transformation by the change in the curve slope. Before and after the martensitic transformation the material has an elastic behaviour, first as austenite and then as martensite. The energy dissipated in every complete cycle is represented by the area between the two curves. For example, while conventional stainless steel accommodates higher stress levels by irrecoverable slip, a superelastic alloy accommodates higher deformation in a reversible process by shifting to twinned martensite [4,9]. The different deformation mechanisms are represented in Figure 2.9.

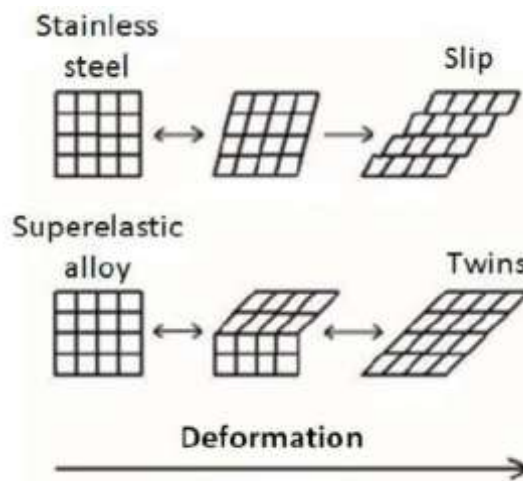


Figure 2.9- Representation of lattice changes in stainless steel and in a superalloy [4].

The superelasticity, as a functional property, makes SMAs interesting for some specific applications when compared to conventional alloys, either for the large recoverable strains, or for the constant stress levels, or both.

NiTi alloys have a very narrow chemical composition gap near equiatomic composition (50 at% Ni – 50 at% Ti), as presented in Figure 2.10. Characteristics such as: SME, SE, damping and impact absorbing are strongly dependent on the stoichiometry which varies with thermal and mechanical treatments [10].

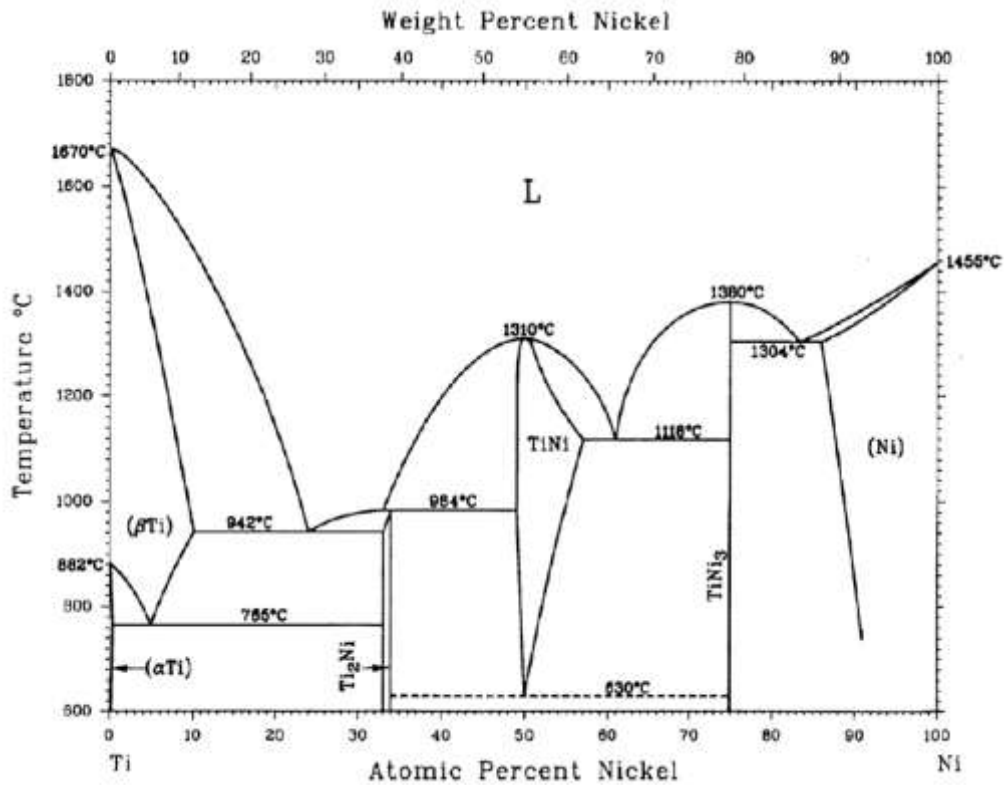


Figure 2.10- Ni-Ti phase diagram [10].

NiTi alloys can have transformation temperatures below -100 °C and up to +100 °C and small variations of the alloy composition originate significant variations on its transformation temperatures. As an example, a variation of 0.1 at. % in the Ni content is shown to shift the transformation temperatures by nearly 10 °C (Figure 2.11). Impurities such as oxygen, nitrogen and carbon should also be avoided since the transformation temperatures, hysteresis loop, strength, and ductility of the material are very sensitive to these impurities.

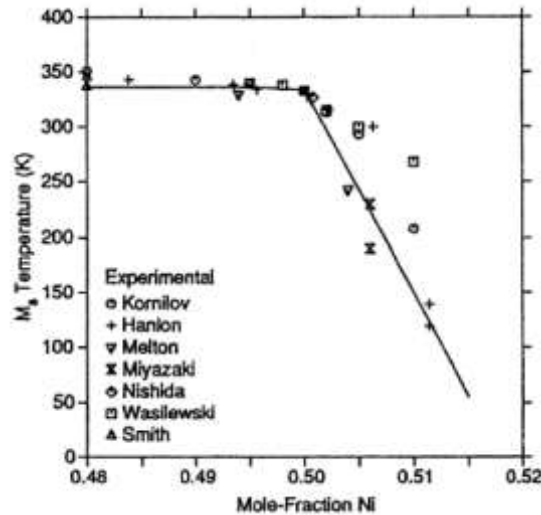


Figure 2.11- Variation of transformation temperature with Ni content for binary Ni-Ti alloys [7].

For the optimization of SMA properties it is imperative to have detailed knowledge of the transformation characteristics of the alloy and its correlations with chemical compositions and treatment processes (thermal, mechanical or thermomechanical).

2.3 - Welding processes of Shape Memory Alloys

SMAs present poor workability when conventional machining processes are used [11]. Thus, to obtain more complex components, suitable joining techniques have to be developed. Unlike common alloys, welding SMAs presents multiple challenges, due to the fact that SMA properties are strongly dependent on the chemical composition. So, joining SMA demands minimal modification of the weld bead composition when compared to the base material, in order to avoid significant alteration to the alloy's properties. Despite the large number of existing welding processes, laser is by far the most investigated. Since this study concerns TIG welding, this chapter just presents the two processes.

2.3.1 - Gas Tungsten Arc Welding - GTAW

Gas Tungsten Arc Welding (GTAW) also known as Tungsten Inert Gas (TIG), is a gas-shielded arc welding process that uses a non-consumable tungsten electrode to establish the electric arc with the material to be welded. This generates heat, promoting the formation of a weld pool. The weld pool is protected from air contamination by an inert gas atmosphere of Ar or He [3,12,13].

Autogenous TIG welding, that is without filler metal (Figure 2.12) is used in thin square sections edges, up to 2 mm thick plates, while for thicker sections, V and X edge preparations are needed, together with a filler metal. GTAW process is extensively used in

precision welding where good quality is required, mainly to weld thin components of stainless steel, aluminium, magnesium or titanium alloys, where oxidation has to be prevented [3,12,13].

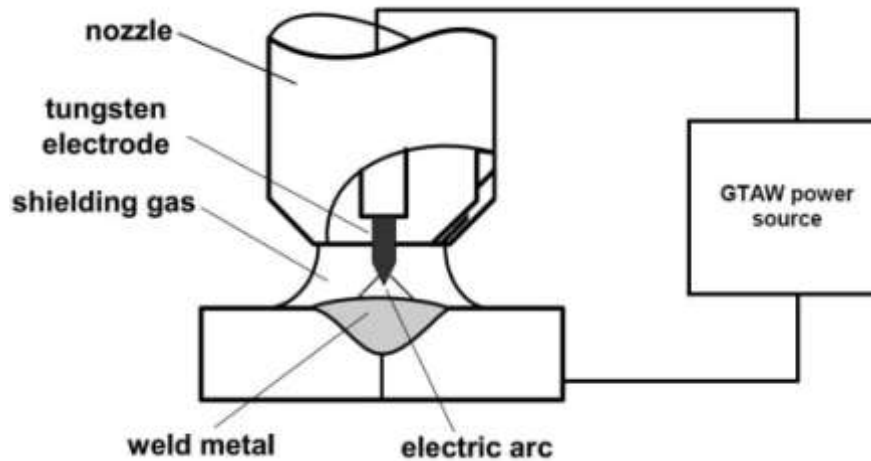


Figure 2.12- Autogenous Gas Tungsten Arc Welding (GTAW) process representation (Adapted from[12]).

The process can be used with: direct current electrode negative (straight polarity); direct current electrode positive (reverse polarity); and alternating current. Each current type has its applications, advantages and disadvantages. The penetration pattern as well as the weld bead configuration are directly correlated with current type selection [12,13]. The characteristics of each configuration are presented and summarized in Table 2.1.

Direct Current Electrode Negative (Straight Polarity)

Direct Current Electrode Negative (DCEN) is the most common polarity used in GTAW to weld, practically, all metals, except aluminium and magnesium. In DCEN polarity, the torch is connected to the negative terminal of the power source, being the workpiece connected to the positive terminal. Thus, when the arc is established the electrons flow from the electrode to the workpiece. Since in a direct current (DC) the welding arc concentrates approximately 70% of the heat, a great amount of heat is distributed into the workpiece, leading to a deep penetration of the weld beads [12].

Direct Current Electrode Positive (Reverse Polarity)

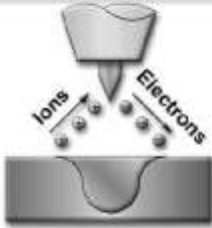


In Direct Current Electrode Positive (DCEP), opposite to DCEN, the torch is connected to the positive terminal and the workpiece to the negative one. In this case, the electrode is the one under a large amount of the total heat, being necessary to use wider electrodes, even for low amperage, to avoid overheating and possible melting of the electrodes. As a

consequence, the workpiece has less heat resulting in a shallow penetration of the weld bead. This mode is mainly used to weld aluminium and magnesium alloys because it provides a cleaning action of the base material breaking and removing surface oxides [12,13].

Alternating Current

In order to obtain the advantages of both DCEN and DCEP, namely: good cleaning action and good penetration, alternating current is used. In this case, the terms of positive and negative applied to the electrode and workpiece are not considered since the current/polarity is always alternating, the flow direction, operating in cycles. During a complete cycle there is one half cycle when the electrode is positive and another in which it is negative, as the workpiece has opposite signal of the electrode [12,13].

Table 2.1- Characteristics of current types for Gas Tungsten Arc Welding.

Current Type	DCEN	DCEP	AC (Balanced)
Electrode Polarity	Negative	Positive	
Electron and Ion Flow			
Penetration Characteristics			
Oxide Cleaning Action	No	Yes	Yes-Once Every Half Cycle
Heat Balance In The Arc (Approx.)	70% At Work End 30% At Electrode End	30% At Work End 70% At Electrode End	50% At Work End 50% At Electrode End
Penetration	Deep; Narrow	Shallow; Wide	Medium
Electrode Capacity	Excellent 1/8" (3.2mm) 400 A	Poor 1/4" (6.4mm) 120 A	Good 1/8" (3.2mm) 225 A

Pulsed Mode

In pulsed mode, the welding current changes from high (peak) amperage to a low (background) amperage rapidly and repeatedly. The amperage peak provides the melting of the workpiece, while the background amperage is enough to keep the electric arc, allowing the work piece to cool and solidify. The weld bead attained is characterized by discontinuous weld points, overlapping each other in about 50% of their length. This mode is able of welding over a wide range of joints with geometrical variations and in automatic process where problems regarding heat input such as: lack of penetration or burn throughs, can be minimized [12,13].

The welding speed also modifies the weld bead shape. For the same current intensity and voltage, increasing the welding speed results in a decrease of the heat input, hence producing a small weld bead.

The heat input (H) is a measure of the energy transferred from the arc to the workpiece per unit length of a weld. It is an important parameters because, like preheat and interpass temperature, it influences the cooling rate, which may affect the mechanical properties and metallurgical structure of the weld and the Heated Affected Zone (HAZ). Heat input is typically calculated as the ratio of the power to welding speed velocity of the heat source as follows:

$$H = \frac{V \cdot I}{s} \times \eta \quad (2.1)$$

Where,

H – Heat input (J/mm)

V – Arc Voltage (V)

I – Current (A)

s – Welding Speed (mm/min)

η – Heat Transfer Efficiency (%)

The heat transfer efficiency(*η*), can be determine experimentally by calorimetry or taken from available data which in the case of TIG is of 0.7 %.

TIG welding allows a precise control of heat input and heat addiction providing superior qualities welds, with low distortion and free of spatter. Although heat input is small when compared with other arc welding processes, it presents an heat input about ten times higher than laser welding, causing extended heat affected zone (HAZ) in the welded sample [3,12].

2.3.2 - Laser Welding

Laser beam radiation is a coherent and monochromatic beam of electromagnetic radiation produced by stimulated emission. In fact, LASER is an acronym for Light Amplification by Stimulated Emission of Radiation.

Laser welding is based on the principle that when a laser beam is focused on the material surface through an optical system, it increases the temperature, leading to the

melting of the work piece, providing the joint upon cooling. The effectiveness of the beam coupling depends on the wavelength of the beam radiation and the optical properties of the material, including the surface conditions. There are two fundamental modes of laser welding depending on the power density, focal joint position and the beam mode, represented in Figure 2.13: (a) "keyhole" or penetration welding and (b) conduction welding [1,6]. Both modes can occur simultaneously in a joint.

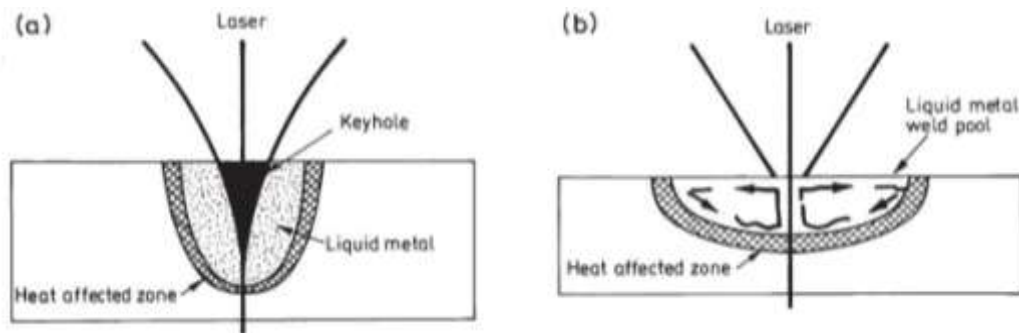


Figure 2.13- Laser welding modes: a) "keyhole" and b) Conduction [14].

In a "keyhole" laser welding mode, high power density is used for material joining, leading to the formation of a cylindrical cavity of metallic vapour throughout the material thickness. The cavity is sealed up by the molten walls as the process progresses. The weld is characterized by a parallel sided fusion zone and a narrow width. Conduction laser welding is obtained for low power density, where most of the beam energy is lost by reflection. The energy absorbed by the material is below a threshold value, sufficient to melt the material but not enough to vaporize it, leading to heat conduction into adjacent regions. Conduction mode is characterized by a wide and low penetrated molten pool, similar to TIG welding. [3,6,14]. Recently [15] found that this mode has advantages over keyhole since the thermal gradient is not so steep, which can be useful in difficult to weld materials and in dissimilar joints.

2.4 - NiTi Similar Joints

Most of reported studies dealing with welding and joining of SMAs concern laser welding, since arc welding processes commonly produce welds with extended HAZ, not desirable in most cases. Limited information can be found regarding welding SMA using arc welding techniques. Ikai [16] successfully performed microwelds on NiTi thin wire (outer diameter of 0.75 mm) and sheet (0.2 mm thickness) using TIG welding, but significant degradation of weld mechanical properties was observed.

Previous work, developed by Vieira [1] on laser welding of similar NiTi joints, the welds with better mechanical properties were the ones with larger weld bead width on

the face and in the root that is with low aspect ratios typical of a conduction weld. These are marked in figure 2.14 with an arrow.

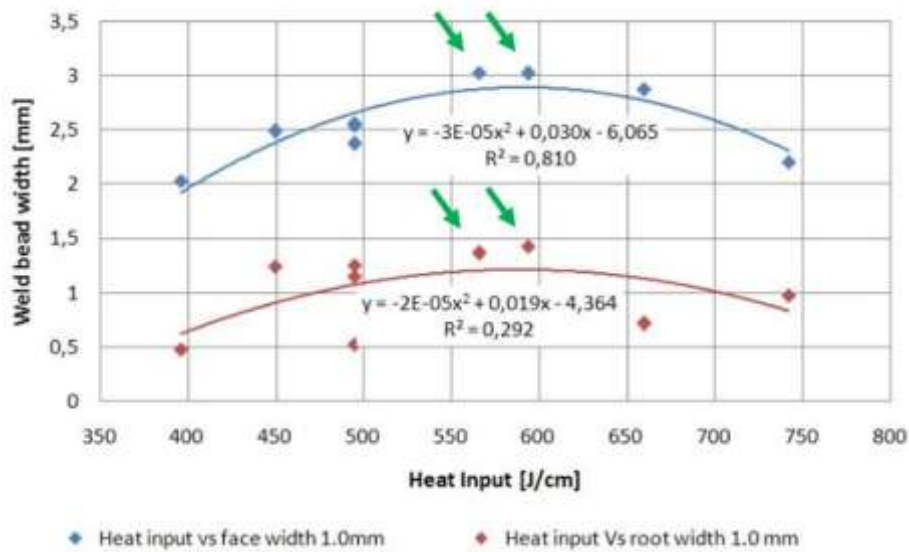


Figure 2.14 - Relation between heat input and the weld bead face and root width. Adapted from [1].

2.5 - Applications

Shape Memory Alloys characteristics and functionalities present a vast interest for a wide range of industries. Since their discovery a large number of patents have been issued for every conceivable application using SMA. However, only few applications have had commercial success. The lack of knowledge and technology available to overcome technical difficulties associated to SMAs were the main reason [1,8,17].

NiTi alloys are the most used SMA in applications and devices. In addition to SME and SE, NiTi alloys exhibit useful characteristics in terms of its active temperature range, hysteretic performance, recoverable strain, relatively simple thermal processing and biocompatibility, making them preferable over others SMAs. NiTi alloys are commercially available, but its production is in a much smaller scale compared to conventional metals and alloys, due to difficulties associated with production processes. Despite the setbacks related to production and workability over the past decades, with technology advancements and new studies, SMAs have attracted a great deal of interest in various fields of applications ranging from aerospace and naval to surgical instruments, medical implants and fixtures [1,8,17].

2.5.1 - Aerospace Applications

Aerospace industry is known for demanding state of the art materials and technologies. Smart materials lead to new design concepts, allowing fully integrated and distributed actuation by means of simple mechanisms that do not add weight. SMA technology is implemented in the aerospace industry, with great success, and has been used for areas such as: fixed-wing aircraft, rotorcraft and spacecraft. Despite previous achievements the work in all these areas is still progressing [1,8].

Fixed-Wing Aircraft Applications

There have been a number of other efforts to integrate SMA elements into aerostructures.

Engine noise levels during takeoff and landing have become more highly regulated worldwide. To reduce this noise, some designers are installing chevrons onto engines to mix the flow of exhaust gases and reduce engine noise. Research is being performed into methods by which SMA beam components can be embedded inside chevrons (Figure 2.15). The SMA beams bend the chevrons into the flow during low-altitude flight or low speed flight, thereby increasing mixing and reducing noise. During high-altitude and high speed flight, these SMA beam components will cool into martensite, thereby straightening the chevrons and increasing engine performance [8].



Figure 2.15 - Variable geometry chevron [8].

Many other applications are being studied. Another example, is one project where a variable geometry airfoil was developed and through SMA actuation it was effectively possible to change its configuration from symmetric to cambered [8].

Rotorcraft

The role of SMAs in rotorcraft applications has been focused on the main rotor. The research is based on actuating SMA blades. These SMA blades, when actuated, could twist and facilitate the formation of different blade configurations and thereby optimize performance of such aircraft in both the hover and forward flight regimes.

SMAs are ideally suited for such applications because of their high actuation energy density and forces required in the small available volume within a rotor blade [8].

Spacecraft Applications

SMAs have been used in space applications to address problems related to actuation and release in zero atmosphere environment as well as vibration damping during spacecraft launch.

One such application that uses SMAs is for the low-shock release mechanism in satellites. Some space missions experienced failure due to shock caused by the pyrotechnic release mechanisms, in some cases, causing the mission to be aborted. The slow actuation due to gradual heating in SMAs makes them suitable for low shock release mechanisms in space applications, in this case the SME is used [8].

SMAs are also used in actuation of various components such as solar panels. The Lightweight Flexible Solar Array (LFSA) used thin SMA strips as hinges, which deploy the folded solar panels upon heating in approximately 30 seconds [8]. The concept design is shown in Figure 2.16.

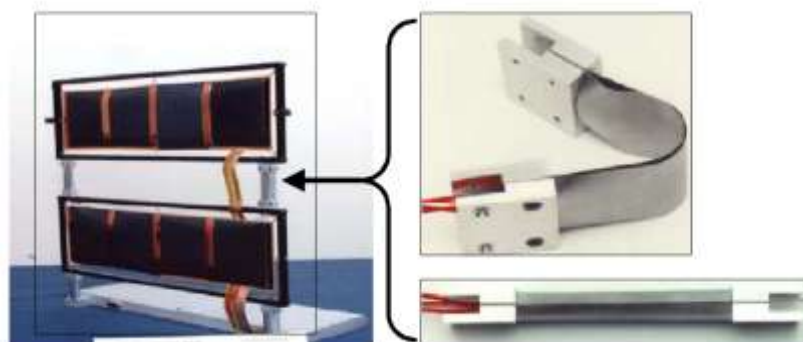


Figure 2.16 - SMA hinges. Folded and deployed configuration [8].

In addition to actuation, another attractive application for SMAs is vibration isolators and dampeners. The hysteresis in the superelastic behaviour is representative of the mechanical energy that an SMA can dissipate during a cycle. Further, the change in the

stiffness from the initial elastic region to that in the transformation region makes it an effective tool to isolate vibrations [8].

2.5.2 - Medical Applications

NiTi alloys properties such as SME and SE characteristics combined with biocompatibility make them an attractive material medical applications. The combination of these properties has lead to the development of various applications, from stents to orthodontic wires, as well as devices for minimal invasive surgery [8].

Orthodontic Applications

The properties of SMAs have been successfully implemented in a variety of dental applications. Since the 1970's NiTi orthodontic archwires have been used for being more effective than other alternative materials (Figure 2.17 - a)). Combining NiTi with other materials allows obtaining selective components that are able to control the force applied on each teeth, resulting in a more effective solution. Another dental application for SMAs involves the use of NiTi drills used in root canal surgery, which involves careful drilling within the tooth (Figure 2.17 - b). The Nitinol drills can bend to rather large angles, which induce large strains, yet still withstand the high cyclic rotations [1,8].

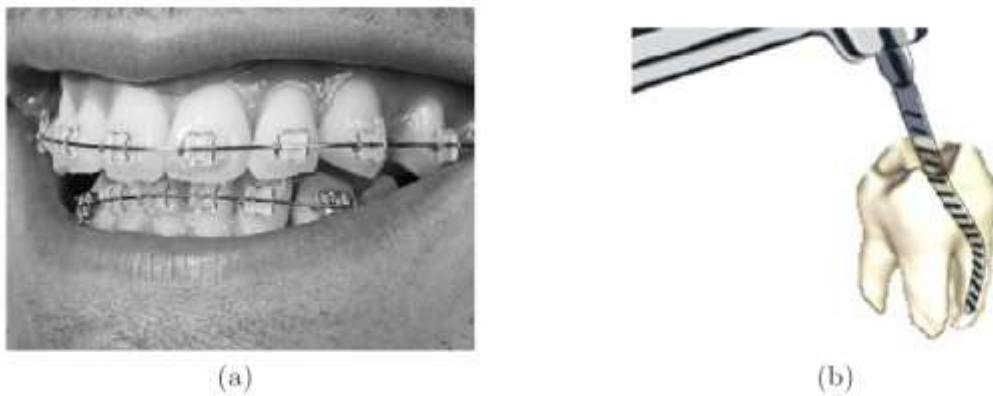


Figure 2.17 - Orthodontic applications of NiTi SMA: a) NiTi braces; b) schematic of a NiTi drill used for root canal surgery [8].

Cardiovascular Applications

One of the first cardiovascular SMA device was the Simon Filter, as represented in Figure 2.16 - a). The device acts as a filter that traps to eventually dissolve the clots travelling in the blood stream. The device is deformed and constrained within a catheter. The filter when deployed in the blood vessel and release from the constraint, with the ambient temperature (higher than A_s), expands and assumes its original shape [8].

A more common cardiovascular application is the “self-expanding” NiTi stent. Like other conventional stents, this device is used to support the inner circumference of tubular passages in the body such as blood vessels. Traditionally, stents are made using stainless steel, that could damage the vessel when applied. Self-expanding NiTi stents provide an attractive alternative to the traditional method. After being constrained, the NiTi stent is introduced and released in the artery. There it expands to its original larger diameter and gently pushes outward on the walls, considering that the temperature exceeds the A_s temperature of the stent material. Figure 2.18 - b) shows an illustration of a NiTi stent in the constrained and deployed configuration [8].

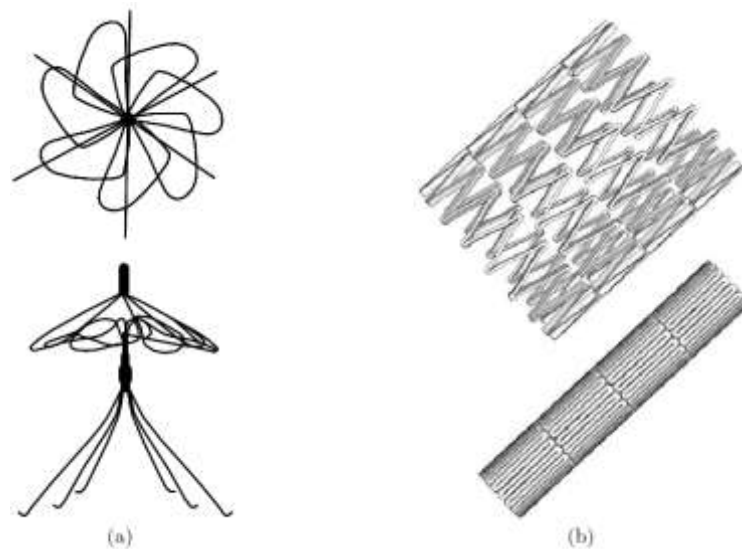


Figure 2.18 - Cardiovascular applications: a) Simon's filter in deployed configuration; b) Self-expanding NiTi stent [8].

Surgical Instrument Applications

Advances in medicine continue to enhance the use of minimally invasive surgery (MIS). Some of the enabling technologies advancing MIS includes instruments that can be inserted through these small openings followed by expansion to a desired size for the particular function. The superelastic and shape memory effect properties of SMAs allow for more creative design options compared to conventional materials. One such device is the SMA basket used to remove stones in the bile duct. Other instruments using the shape memory effect behaviour include surgical tools with grippers, scissors and tongs used in laparoscopy procedures. Superelastic guide wires are widely used in surgery due to their kink resistance and superior flexibility [8].

2.5.3 - Transportation Applications

Shape memory alloys have been used in automobiles for applications ranging from impact absorption to sensing and actuation. The superelastic behaviour hysteresis provides an effective system to dissipate vibrations and impact, and has been used for impact absorption on armour vehicles in military and commercial applications. The SME has also been implemented for remote opening and closing of louvers on automobile fog light to prevent damage from the road debris. A series circuit ensures the actuation of the SMA louvers every time the fog lamps are turned on [8,17].

SMAs can also be used for sensor and actuation purposes simultaneously. An application that exploits this behaviour is the SMA spring for the continuous variable transmission in the Mercedes A class. The spring acts as a sensor that monitors the temperature and actuates a valve at a specific temperature, which changes the direction of oil flow. A similar actuation system is incorporated in the Shinkansen bullet train gearbox where the temperature in the gear box is monitored and an SMA spring actuates a valve to adjust the oil level in the gearbox. Other applications developed for trains include the thermally actuated switch for the radiator fan in diesel engines and steam traps for the steam heating system in passenger trains. Both of these applications utilize the shape memory effect [8].

2.5.4 - Other Applications

There are many other fields and applications that incorporate and take advantage of SMAs characteristics.

In everyday applications such as coffee makers and rice cookers SMAs can be incorporated. A rice cooker can be equipped with an SMA valve that actuates when the cooker reaches a certain temperature releasing the excess steam in the chamber. SMA actuated louvers can also be incorporated in air conditioning vents that can adjust depending on the temperature of the air exiting the vents. The SME is also utilized in shower faucet designs where an SMA spring automatically adjusts the flow of hot and cold water to maintain a preset water temperature. The superelastic behaviour has also been used in a wide range of applications. Developers of vibration control devices in civil structures have shown interest in superelastic behaviour of NiTi due to its capability to dissipate energy through a large hysteresis. Other applications that employ the superelastic behaviour are flexible metallic eyeglasses and headphones, that can be bent without breaking. SMAs have also been used in sporting goods like golf clubs where the SMA embedded in the club absorbs the impact of the strike [8].

The possibility to use SMA in different patterns and produce complex shape changes such as rolling, spiralling, arching and folding, can open prospects for other novel design applications using SMAs [1,8].

2.6 Summary

In this chapter it was described the characteristics and the technological interest of shape memory alloys, specially NiTi. The mechanism involved in both SME and SE have been addressed. The possibility to join this material would open up new possibilities to manufacture complex components without losing either shape memory effect or superelasticity.

Two welding processes have been described: laser and TIG. Both processes have low heat inputs, limiting the material transformation in the heat affected zone, though laser welding has a higher density than TIG.

Also, a few application using SMAs are presented showing the vast areas of technological interest for SMAs.

3 - EQUIPMENT DEVELOPED

This chapter describes new pieces of equipment designed and manufactured to produce the welds and the adaptations introduced in the weld source. Also, existing equipment for shape memory effect evaluation had to be adapted for this study.

3.1 - Positioning Device

To assure the plates position for welding, a special jig was designed and manufactured based on the following functional requirements:

- To allow a tight fit of the samples for butt welding;
- To assure, a good shielding gas in the face and in the root to prevent oxidation since NiTi easily oxides at temperatures above 500 °C;
- To facilitate welding fumes to escape;
- To enable process visualization.

The positioning device consisted in two distinct parts:

- A stainless steel base, with a central canal to feed the weld root with shielding gas, where two position rulers were mounted (Figure 3.1). The feeding of the canal was done

underneath by a stainless steel tube welded to it, so the base bead had to be elevated. Near the exit of the gas flow protection a diverter was necessary to avoid direct contact of the gas flow with the weld still molten. The base also was elevated to allow the assess of the shielding gas feeding tube.

- A chamber to contain the shielding gas, with a trapezoidal prism shape, open on the top, to allow the weld fumes to escape (Figure 3.2). This chamber was also made in stainless steel while the lateral faces were made from transparent acrylic, to enable the process visualization.



Figure 3.1- a) Top view of the base - central canal and position rulers mounted; b) perspective view of base with position rulers mounted.



Figure 3.2- Welding chamber.

The technical drawings are presented in annex A.

3.2 - Trigger Device

Since the welding torch had to be manually activated during the entire welding process, two major problems were detected with the TIG welding machine: speed variation of the torch and variation of the distance of the tungsten electrode to the welding plate. Both problems identified were due to pressure variations done on the activation button. As a solution, a small trigger device was developed to avoid disturbance on the torch and also to assure that the process would be consistent and repeatable. The device developed consisted on an ON/OFF switch with the purpose to activate and deactivate the torch. The device was manufactured using a 3D printing machine.

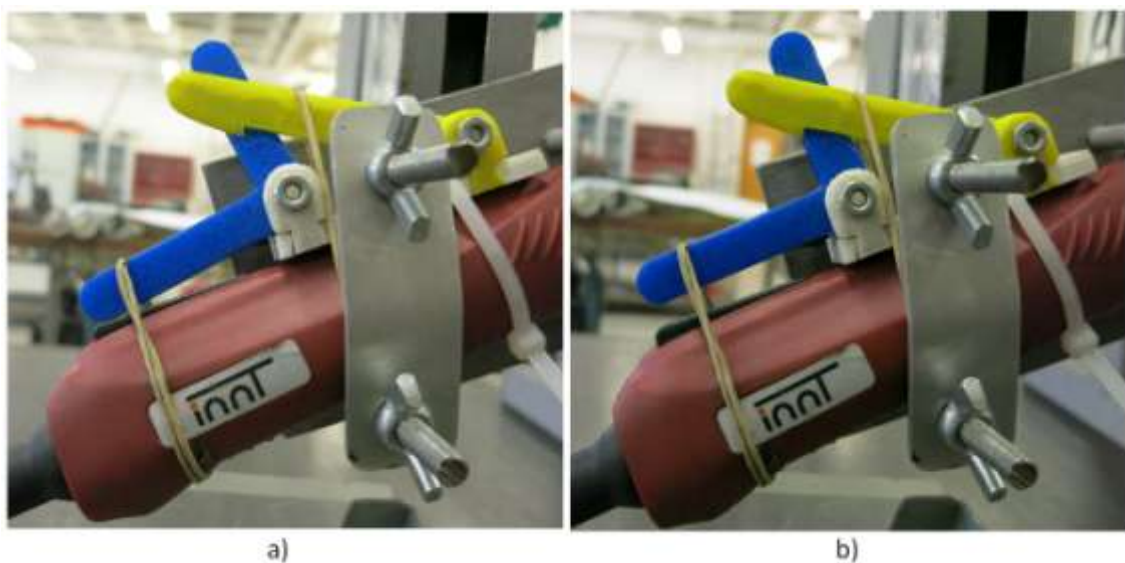


Figure 3.3 - Trigger device: a) ON; b) OFF.

The technical drawings which depict of the trigger device are presented in annex B.

3.3 - Adapted Equipment

3.3.1 Moving Table

In order to guarantee repeatability of the welding conditions and parameters an existing moving table developed for metal arc welding [18] was adapted to TIG (Figure 3.4) in order to keep constant the welding speed and the distance between the weld electrode and the pieces to be welded. For this a program was developed in *Labview* which could control the direction of the welding torch and turn ON/OFF the equipment. (Figure 3.5). The welding speed was controlled by a *GW Instek: GFG-8020 M Function Generator* (wave

generator) making the program suitable for any computer. The program also recognized the limit sensors installed, to avoid damaging the structure while operating.



a)

b)

Figure 3.4 - X-axis Table: a) over view of table; b) set up.

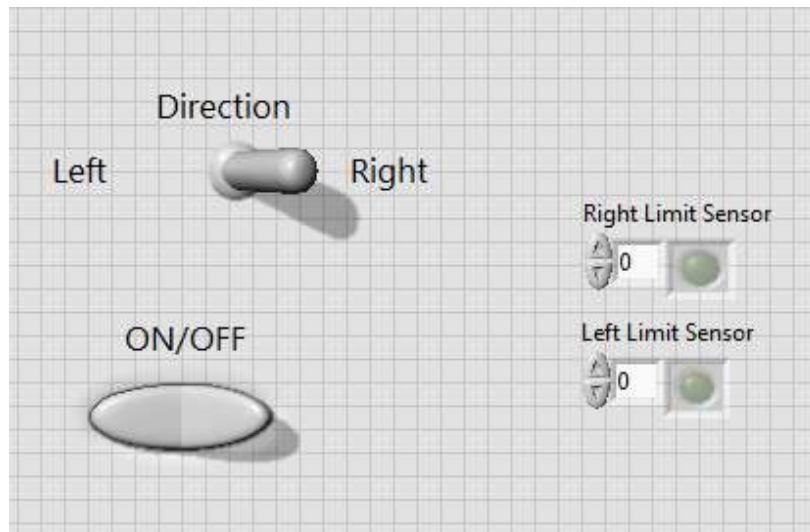


Figure 3.5 - Robot arm control program interface.

3.3.1.1 Testing Device For Shape Memory Effect Evaluation

The testing device (Figure 3.6) for SME evaluation was previously developed by Vieira [1] for 1 mm thick plate samples.

Since the material used in this study had 1.5 mm thickness, the device had to be modified to allow testing plate thicknesses from 0.5 to 2.0 mm, or wires up to 2.0 mm of

diameter. Machining of the existing device was performed to accomplish with these requirements and is shown in Figure 3.7.



Figure 3.6- Device used for shape memory effect testing.



Figure 3.7 - Shape Memory Effect device after modifications.

4 - EXPERIMENTAL PROCEDURE

This chapter is divided in three subthemes, each one concerning:

- Materials - properties of the material used throughout the study are described, as the samples shape and dimensions.
- Welding Equipment.
- Experimental approach – description of the procedures used to perform similar NiTi joints in butt weld configuration, as well as the techniques used to characterize the weldments.

4.1 - Materials

In this study NiTi was used, with a composition of 50.8 at.% Ni, to make similar NiTi/NiTi butt joints. The plates had 1.5 ± 0.1 mm thickness from Memory-Metalle GmbH Alloy S (superelastic standard alloy) had an austenitic finish temperature of about 0 °C, flat annealed and surface oxide free. General physical and mechanical properties of the alloy are displayed in Tables 4.1 and 4.2, respectively.

Table 4.1- Physical properties of NiTi SMA [19].

Physical properties of NiTi SMA						
Melting point [°C]	Density [kg/dm ³]	Coefficient of thermal expansion [x10 ⁻⁶ K ⁻¹]		Thermal conductivity [W/m. K]		Specific heat [J/kg. dm ³]
		Martensite	Austenite	Martensite	Austenite	
1300	6.45	6.6	11	8.6	18	322

Table 4.2- Mechanical properties of NiTi SMA [19].

Mechanical properties of NiTi SMA						
Young modulus [GPa]		Ultimate tensile strength [MPa]		Elongation [%]		Poisson ratio -
Martensite	Austenite	Cold worked	Hot worked	Cold worked	Hot worked	
70-83	28-41	1900	895	5-10	25-50	0.33

The NiTi plates were cut into squares of 30x30 mm sample, using a precision cut-off machine ATM GmbH model Brilliant 221, equipped with a diamond wheel type B102 from the same maker. Cutting parameters were:

- Speed: 3500 rpm;
- Feed rate: 1 mm/min;
- Lubricant: multipurpose cutting fluid.

After cutting the samples were hand finished and chemically cleaned using a solution of 10% HF + 45% HNO₃ + 45% H₂O to remove cutting moisture contamination and surface oxides prior to welding.

4.2 - Welding Equipment

A TELWIN, TECHNOLOGY TIG 182 AC/DC-HF/LIFT (Figure 4.1), was used to produce the welds. The main characteristics of the GTAW equipment are presented in Table 4.3.



Figure 4.1- TELWIN, TECHNOLOGY TIG 182 AC/DC-HF/LIFT.

Table 4.3 - TELWIN, TECHNOLOGY TIG 182 AC/DC-HF/LIFT Technical Data [20].

Code	815332
Current range	5 - 160A
Max. current (40°C)(EN60974-1)	160A 20%
Current at 60% (EN60974-1)	85V
Max. no load voltage	94V
Absorbed current	18 - 29 A
Absorbed power	2.5 - 4.3 kW
Efficiency	75%
Power factor	0.7 cosφ
MMA electrode diameter	1.6 - 3.2 mm
Protection class	IP23
Dimensions (L,W,H)	430x170x340 mm
Weight	9.7 Kg

4.3 - Experimental Approach

4.3.1 - Butt joints

Preliminary tests were made on 2.0 mm thick stainless steel plates, to determine processing parameters, including shielding gas flow rate. Commercial stainless Steel (AISI 316) was used since it is a less expensive material than NiTi and has similar thermal conductivity coefficient.

Using direct current (DC) and straight polarity and Argon (98%) as shield gas, several tests were performed to have good welds with full penetration, good surface aspect and free of oxides.

A pure tungsten non consumable electrode was used with 2 mm diameter.

Welding parameters were varied keeping the welding speed constant at 20 cm/min. The gas flow was kept at 15 l/min in the torch, which was the maximum admissible flow that did not interfere with the molten pool and the best flow rate in the root was 12 l/min with a similar objective. So the best parameters are discriminated in Table 4.4.

Table 4.4- Welding parameters chosen to weld the NiTi/NiTi butt joints specimens.

Welding Speed [cm/min]	Electric Current [A]	Heat Input [kJ/cm]	Gas flow	
			Torch [l/min]	Root
20	45 (DCEN)	1.512*	15	8

* According to expression (2.1)

According to Vieira [1], the best mechanical properties were attained with welds performed across the rolling direction, and so were the welds made for this study.

Samples Preparation For Testing

After being welded, the NiTi samples were cut into 3.8 mm wide specimens (Figure 3.12) using the ATM precision cut-off machine for structural and mechanical characterization.

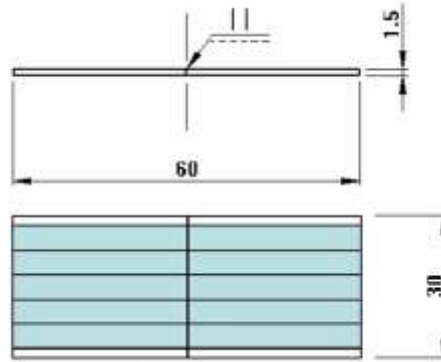


Figure 4.2 - Specimens extracted from welded samples.

Table 3.6 presents specimen reference and characterization tests performed.

Table 4.5 - Specimens references and tests performed.

Sample reference	Specimen reference	Test
#1.1	#1.1.1	8% cycling
	#1.1.2	12% cycling
	#1.1.3	DSC and DRX
#1.2	#1.2.1	SME
	#1.2.2	12% cycling
	#1.2.3	Tensile Test
#1.3	#1.3.1	6% cycling
	#1.3.2	Microscope, SEM/EDS and microhardness
	#1.3.3	7% cycling
	#1.3.4	Tensile Test

4.3.2 - Testing Methods

- Microstructure Observations

Micro and macrostructure were performed on the weld cross-section. The experimental procedure for sample preparation followed previous work developed by Viera [4]. Optical observations were made in an Olympus CX40 microscope, with an Olympus TH3 light source, equipped with a DP21 video camera. Scanning Electron Microscopy (SEM) observations were performed on a ZEISS DSM 962 ESM equipped with an Oxford Instruments INCA-Sight Energy Dispersive X-ray Spectroscopy (EDS) system. Before performing SEM/EDS analyses, the samples were previously coated with gold.

- Differential Scanning Calorimetry - DSC

Differential Scanning Calorimetry (DSC) is a thermal analysis technique that measures the material's heat capacity (c_p) variations with temperature. A sample of known mass is heated or cooled and the changes in its heat capacity are tracked as changes in the heat flow [21].

A DSC 204 F1 Phoenix model from Netzsch was used to perform high and low temperature structural tests and characterize the Base Material (BM), as well as, the weld and the Fusion Zone (FZ), in terms of zero-stress structural transformation temperatures. Liquid nitrogen was used on low temperature tests. Both BM and FZ specimens, were cooled down to -150 °C and heated up to 150 °C. The cooling and heating rate was 10 °Cmin⁻¹.

- X-Ray Diffraction Analysis - XDR

XDR technique was used to analyze separately the phases presented in BM and FZ. With this test, it was suppose determine the phases present in the FZ and to compare these with the ones in the BM.

XRD analysis were performed using a Rigaku DMAX IIIc, 40 kV/30mA, with conventional $\theta/2\theta$ scanning at room temperature and a PANalytical's X'Pert PRO MRD with a geometry of Bragg-Brentano and a Cu K-alpha (wavelength 1.540598 Å) X-rays source.

- Microhardness Measurements

Microhardness measurements were performed along the cross-section of the welded specimen, using a Mitutoyo HM-112 microhardness tester by applying a test load of 500mN. Two Vickers microhardness profiles were made on the specimen, one near the weld root and the other near the top. The indentations done were spaced more than three diagonals from each other and from the boarders.

- Mechanical Tests

Uniaxial Tensile Testing

Uniaxial tensile tests were performed on each welded samples, on an AUTOGRAPH SHIMADZU model AG500Kng equipped with a SHIMADZU load cell type SFL-50kN AG, to

determine the Ultimate Tensile Strength (UTS) and elongation to fracture of the welded sample. The tests were performed at room temperature. A test previously performed on the BM was used as reference for comparison purpose. The chosen specimens are presented in Table 3.7.

Table 4.6 - Uniaxial tensile test specimens.

Specimen Reference	Gauge Length
	[mm]
Base Material	16.30
#1.3.4	32.25
#1.2.3	30.00

Cycling Tests

Using the equipment previously described, cycling tests were performed on 5 different welded samples. These tests allowed the study of the weld's superelasticity behaviour and the analysis of the accumulated irrecoverable strain developed with the increase of the number of completed cycles. The welded samples were subjected to 10 sets of 60 complete cycles, in a total of 600 if the sample did not break. The chosen samples are present in Table 3.8.

Table 4.7 - Cycling test specimens

Specimen Reference	Max. Elongation	Gauge Length
	[%]	[mm]
# 1.3.1	6	31.50
# 1.3.3	7	29.50
# 1.1.1	8	29.50
# 1.2.2	12	35.00
# 1.1.2	12	32.00

- Shape Memory Effect - SME

The SME evaluation of the welded samples consisted on bending and free-recovery testing of the specimen. The method used is described by Vieira [1] and consists on bending a sample in the martensitic condition (at low temperature), removing the load and leaving it at room temperature.

The fundamentals of the test lies on the pure elastic bending theory, synthesized and briefly presented in Figure 3.13 and 3.14, in which the strain varies linearly over the thickness, as presented in equation (4.1).

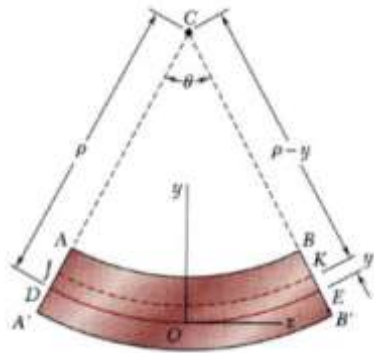


Figure 4.3 - Schema of pure bending [20].

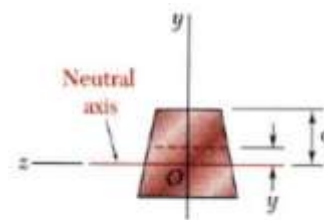


Figure 4.4 - Bending section [20].

$$\epsilon_x = -\frac{y}{\rho} \quad (4.1)$$

Where,

ϵ_x – strain (%)

y – neutral axis (mm)

ρ – deformed diameter (mm)

According to the previous equation 3.1, strain varies linearly over thickness and the highest strain occurs on the inner and outer surfaces. As stated before, the device was modified and had the capability of inducing 3 distinct levels of strain, according to the diameter selected and sample thickness. Considering 1.5 mm thick samples ($y = 1.5$ mm) and the diameter in the middle ($\rho = 22.5$ mm) the strain level induced was 6.7%.

Liquid nitrogen was used to assure that the test was conducted below the parent phase temperature and the bending was conducted using the special mechanism to bend the welded samples. The results are presented as a function of the irrecoverable angle (Ω).

5 - RESULTS AND DISCUSSION

The tests were performed to determine how the welding process would alter the properties of the welded specimen when compared to the BM. The results are presented by the following sequence:

- Preliminary observations of the weld bead;
- Structural observations of each zone of the welded samples (HAZ, FZ and BM);
- DSC analysis to determine the transformation temperature ranges;
- XRD measurements that allow structural characterization of the welded specimens;
- Microhardness measurements done on the transverse sections of the welded specimens.
- Mechanical Tests:
 - Tensile tests to determine the elongation to fracture of the welded sample and the ultimate tensile strength (UTS);
 - Cyclic load/unload of the welded samples and presentation of the evolution of the accumulated irrecoverable strain with the number of cycles;
- SME Evaluation of the welded samples.

5.1 - Macroscopic observations

Similar joints samples are presented in Figure 5.1, where the top and root of the bead from welded samples can be seen.

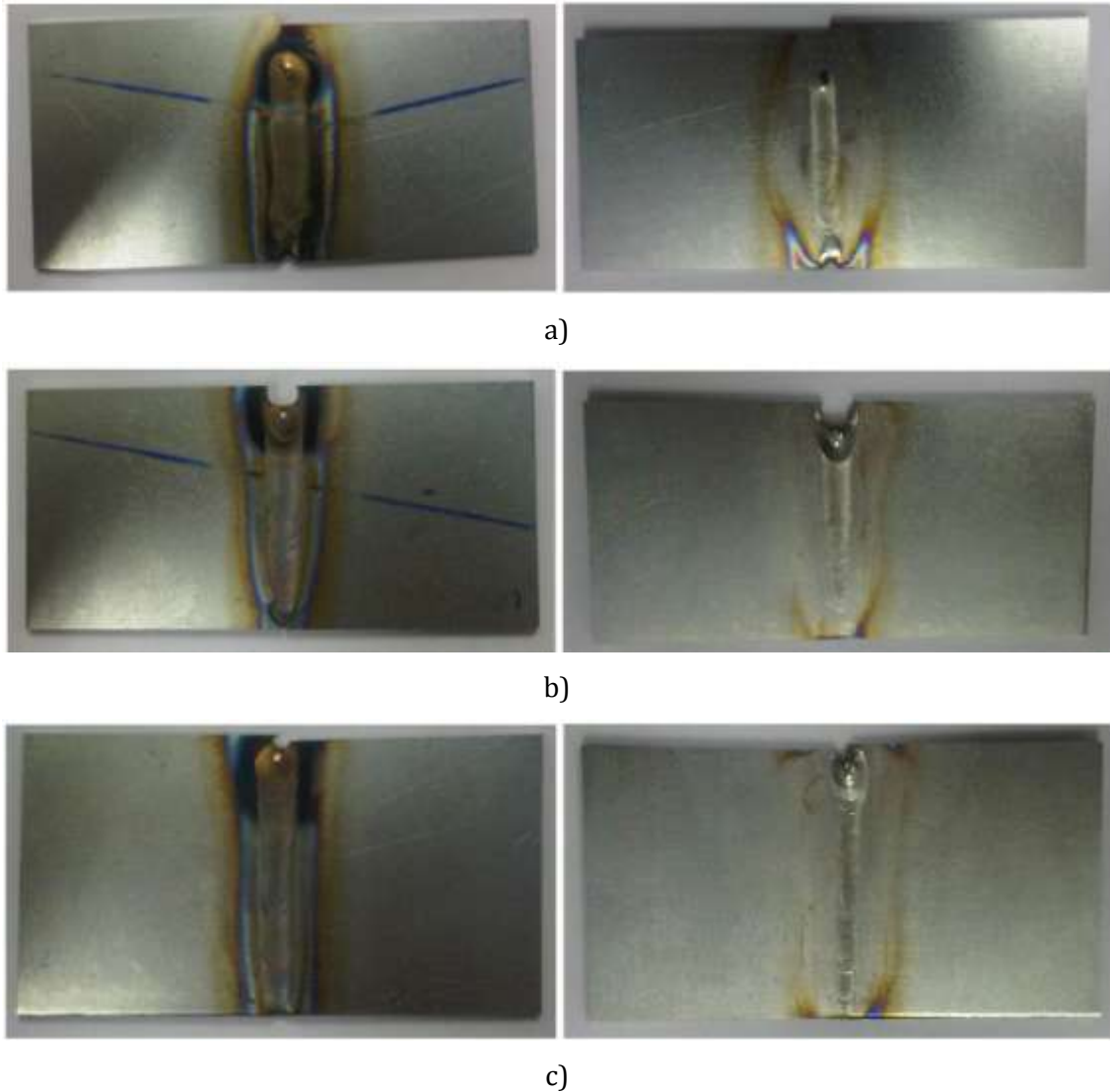


Figure 5.1 - Aspect of similar NiTi butt weld joints: a) sample #1.1; b) sample #1.2 and c) sample #1.3.

It is possible to observe that NiTi/NiTi butt joints were successfully welded. The joints exhibit oxides on the top of the weld and almost surface free oxidation on the weld root. This proves that the root gas feeding system was well designed. No pores or inclusions were visible. Cold cracking was also not detected, as well as other macroscopic defects as lack of penetration or bead irregularities. Figure 5.1 show some aspects of the welded samples.

5.2 - Micro Observations

5.2.1 Microscope Observations

Figure 5.2 depict the microstructure of a weld evidencing the epitaxial crystal growth from the base material into the weld bead. An increase in grain size in the HAZ is evident as shown in Figure 5.3, as well as details of the micro structure of the fusion zone



Figure 5.2 - Specimen microstructure visualization.

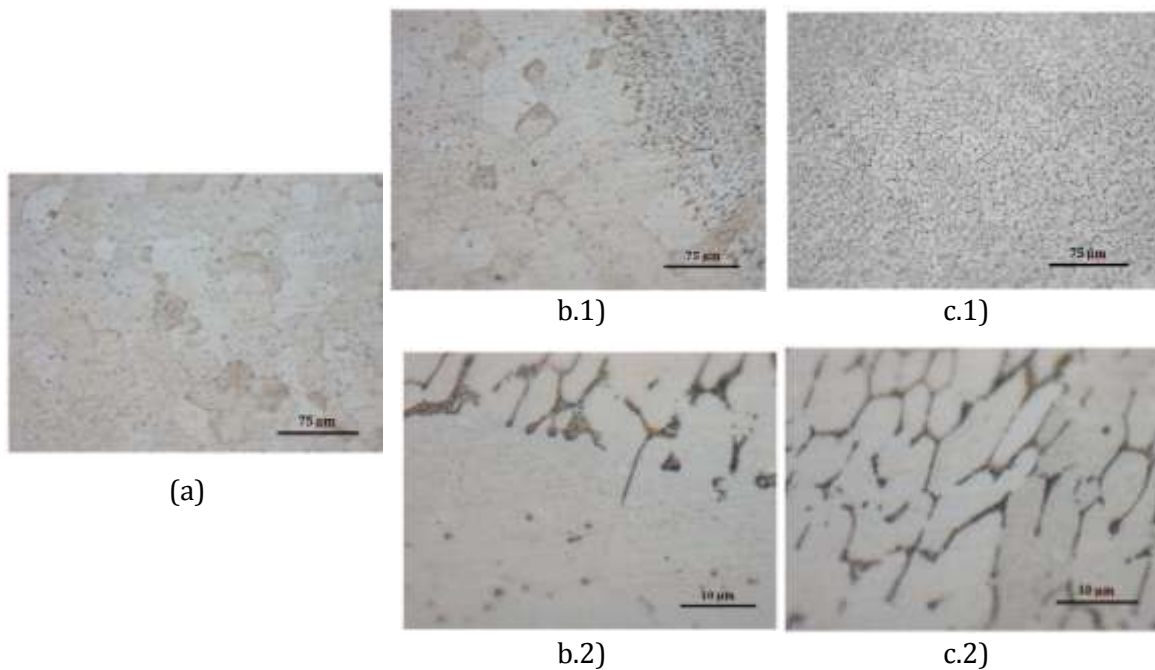


Figure 5.3 - Microstructure of: a) HAZ; b) Transition HAZ/FZ c) FZ.

Figure 5.2 shows a very narrow HAZ due to low heat conductivity of NiTi alloys. Precipitates can be identified in the interdendritic boundaries of primary solidifying

phases as shown in Figures 5.3 b) and c). In the central area of the weld metal a fine equiaxial structure of primary NiTi interdendritic spaces are rich in Ti_2Ni (Figure 5.3 c.2)), due to the volatilization of Ni in these region. In the interface HAZ/FZ, where the cooling rate was higher than in the centre of the fusion zone, the Ni content remained the same leading to an eutectic transformation, forming NiTi + $TiNi_3$ (Figure 5.3 b.2)).

5.2.2 Scanning Electron Microscopy - SEM/EDS

SEM observations were performed on a welded specimen to analyse the chemical composition of the FZ. Since the non consumable electrode was made of tungsten (W), SEM observations also aimed to evaluate the presence of W inclusions in the molten material. These observations were assisted by EDS and the results are depicted in Figures 5.4 and 5.5, for the base material and fusion zone respectively.

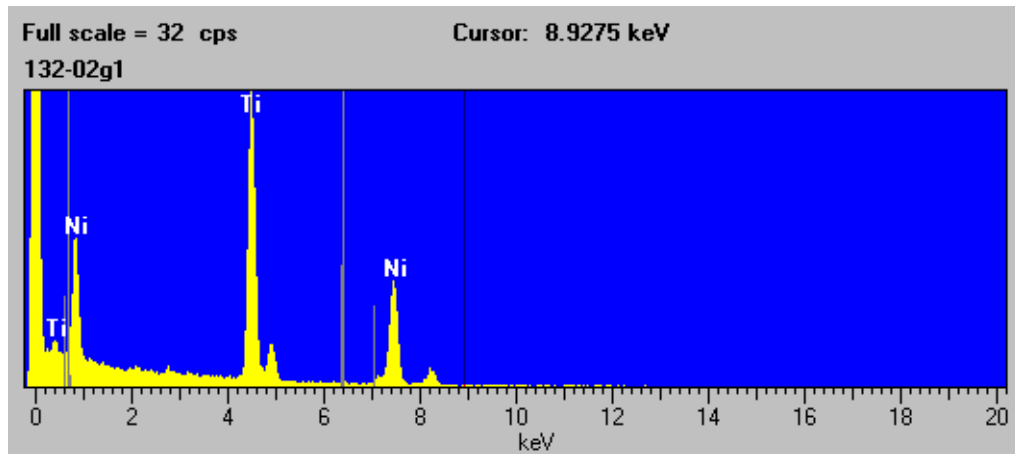


Figure 5.4 - EDS results from Base Material

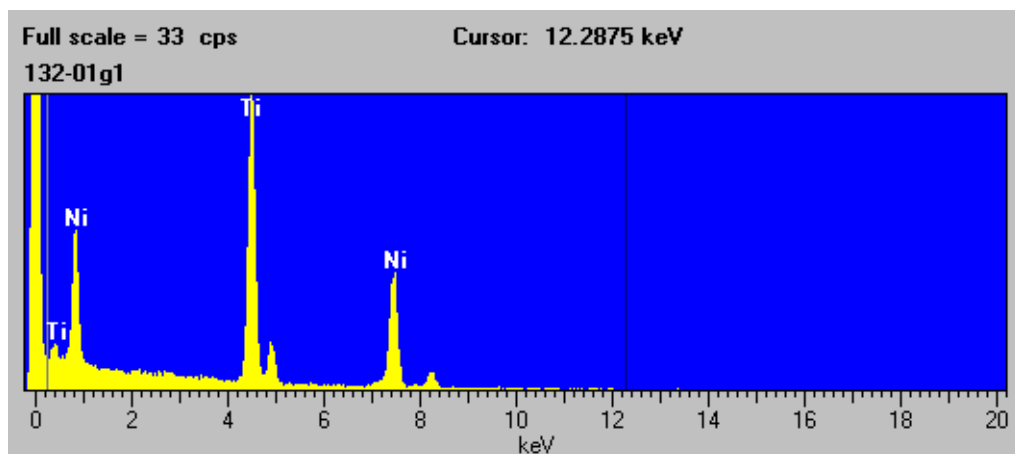


Figure 5.5 - EDS results from Fusion Zone

However, it was observed that the fusion zone had a lower content of Ni when compared to the base material. Table 5.1 shows the variation of the two elements in both

areas. The depletion of Ni observed may be due to the volatilization of this elements under an arc welding process of high temperature. This depletion was expected, since Ni has a higher evaporation rate than Ti [23], as shown in Figure 5.6.

Table 5.1 - Atomic percentage of Ti and Ni on the base material and fusion zone.

	at.%		
	BM	FZ	Variation
Ti	49.09	50.35	+1.26
Ni	50.91	49.65	-1.26

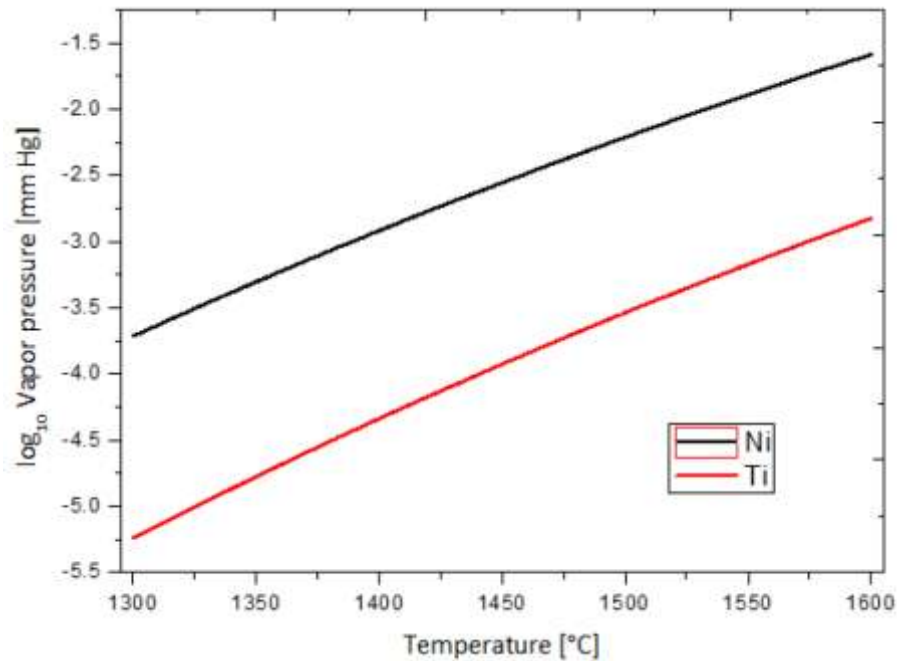


Figure 5.6 - Vapour pressure as a function of temperature for Ni and Ti (Adapted from [6]).

5.3 - Differential Scanning Calorimetry measurements - DSC

Figure 5.7 presents the DSC curves for both the base material and fusion zone and allows to identify the transformation temperatures during cooling and heating condition.

Concerning the base material, a two step transformation upon cooling is identified. B2 structure of austenite changes into R-Phase and from this to B19' martensite. During heating, martensite transforms into austenite. In Table 5.2 a summary of transformation temperatures is given. In the FZ the phase transformations are significantly different from

the BM and B2 structure seems to transform to B19' upon cooling and heating, that is the R-phase is not detected, giving place to a long transformation curve, as shown in Figure 5.9. One possible way to confirm the existence of R-Phase was by performing a XRD analysis with temperature variation in the range of transformation temperatures considered. The long transformation curve, upon heating and cooling, suggests that there is a gradient of transformation temperatures because of the chemical composition gradient along the FZ, due to the temperature variation, from the HAZ/FZ interface to the centre of the weld bead, created by the welding process.

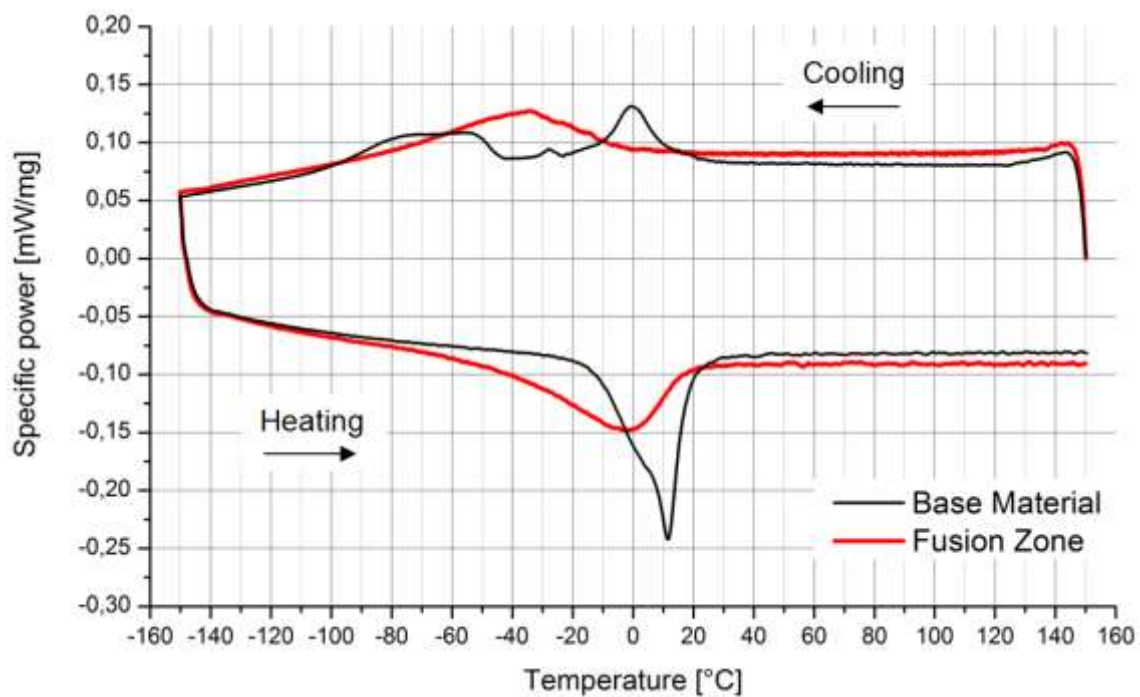


Figure 5.7 - DSC measurements of the base material and molten material for determination of the transformation temperatures.

Table 5.2- Transformation temperatures for base material and molten material.

	R_s	R_f	M_s	M_f	A_s	A_f
	[°C]		[°C]		[°C]	
Base Material	20	-25	-45	-100	-10	25
Fusion Zone	-	-	5	-80	-55	18

As a consequence of the weld M_s and A_s transformation temperatures in the fusion zone are substantially different from those in the base material while the correspondent finishing temperatures have small differences. Another interesting result is that both martensitic and austenite transformations occur over a wider range of temperatures

5.4 - Microhardness Measurements

The indentations profiles made near the top and the weld root, on the cross section of the specimen are presented in Figure 5.9.

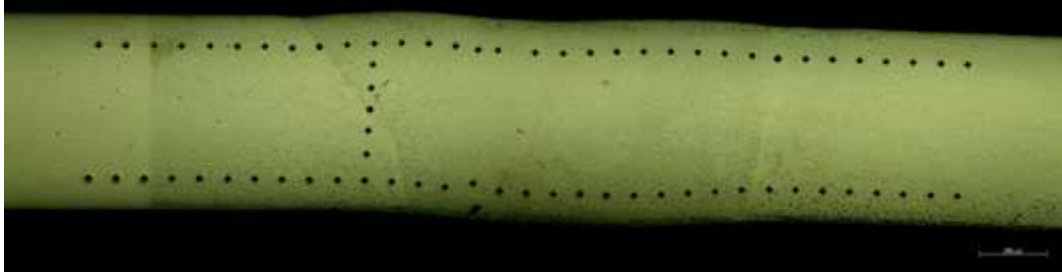


Figure 5.8 - Vickers Microhardness profiles made on specimen #1.3.2.

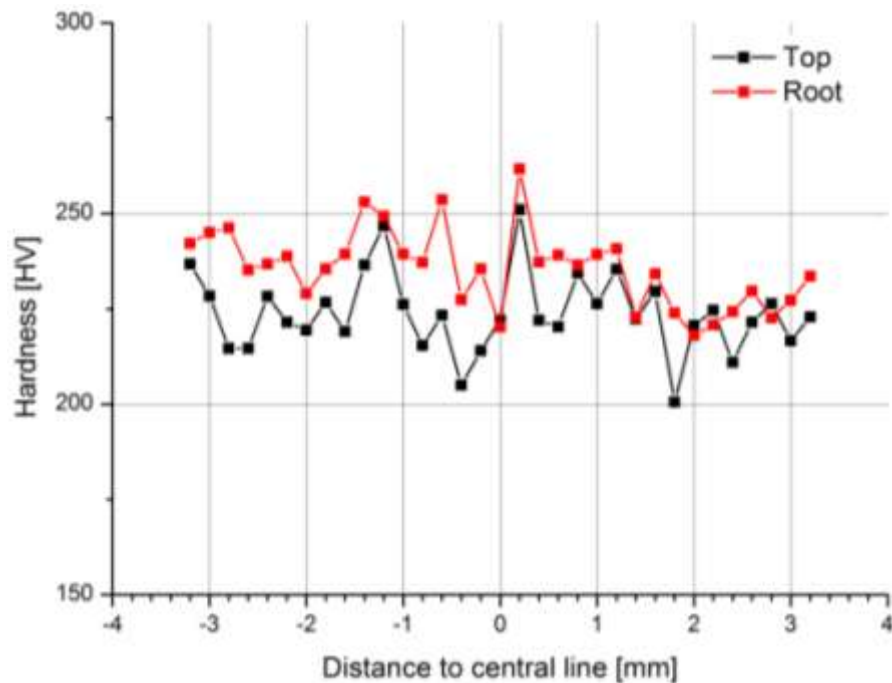


Figure 5.9 - Microhardness measurements in the cross section of the sample along weld top and root.

Despite the slight tendency of the hardness to diminish near the centre of the weld bead, the hardness variations from BM to HAZ to FZ, in both profiles, are not very significant. Near the top, the hardness measurements varied around 220 HV while in the root, the mean values are around 240 HV, eventually due to the existence of precipitates. It is also visible some spikes measurements along both profiles, mainly on the FZ. Variations of 20 to 40 HV can be due to the presence of precipitates, in the FZ, as well as to grain boundaries.

5.5 - X-ray Diffraction Analysis

XDR analysis results from base material and fusion zone, are presented in Figures 5.10 and 5.11, respectively.

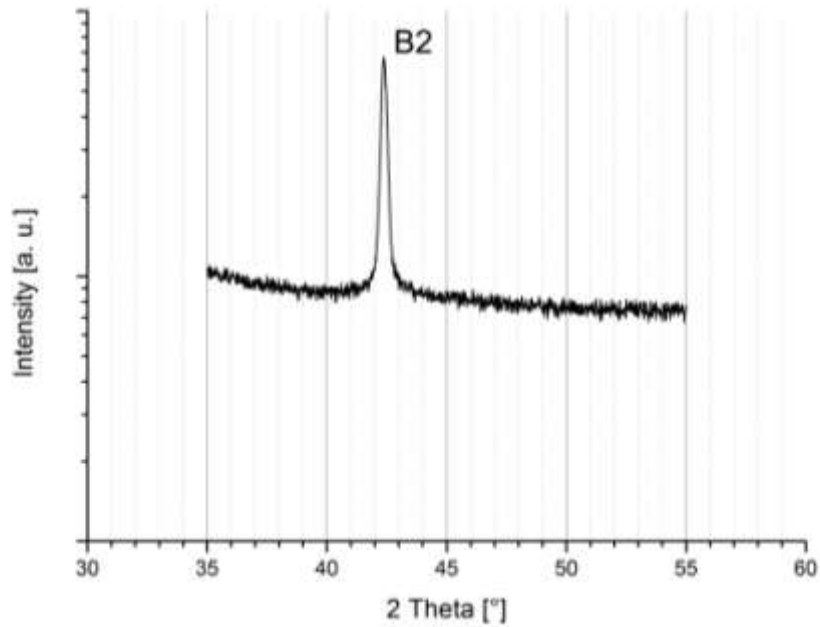


Figure 5.10 - XRD measurements of BM.

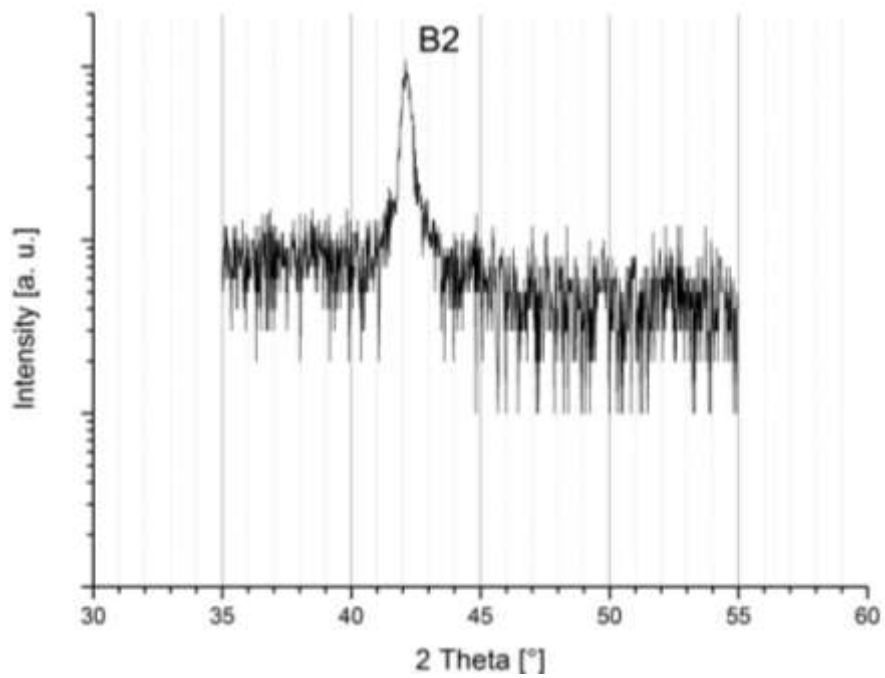


Figure 5.11 - XRD measurements of FZ.

The difference in the spectrums are due to the fact that different equipments were used in this study. The only peak identified corresponds to B2 phase. So the evaluation of the presence of Ni-Ti precipitates in the FZ, regarding microscope observations, was inconclusive. The non identification of the peak may be due to the fact that their content is below the detection limit of the available equipment. Eventually, the peaks corresponding to precipitates are overlapped with back signal noise.

5.6 - Mechanical Tests

5.6.1 - Tensile Tests

Tensile testing up to rupture was performed to evaluate the mechanical properties of the welded sample. With the results, it was possible to conclude that the welding parameters chosen were acceptable and to compare with the results of the BM.

The plots of the tests are presented in Figure 5.12. The Ultimate Tensile Strength (UTS), ductility parameters and superelastic plateau are presented in Table 5.3, for comparison.

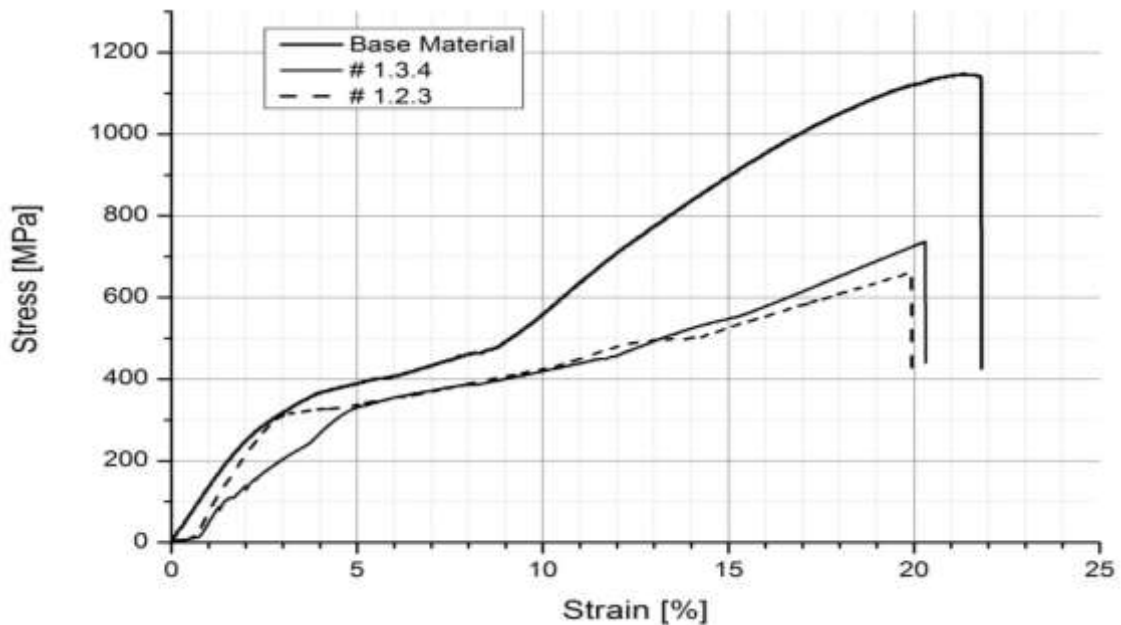


Figure 5.12 - Tensile test performed on Base Material and specimens #1.2.3 and #1.3.4.

Table 5.3 - Uniaxial Tensile test results.

Specimen Reference	Ultimate Tensile Strength (UTS)	Elongation to fracture	Superelastic plateaus	
	[MPa]		[MPa]	[%]
Base Material	1148.1	21.8	350 - 480	4 - 9
#1.3.4	736.9	20.3	320 - 450	2.5-13
#1.2.3	662.3	19.9	310 - 500	4.5-15

As presented in Table 5.3 it is clear that the UTS of the welded sample decreased significantly when compared to the results of the base material. Despite this elongation to fracture is similar to the base material. The superelastic plateau occurs at stress levels of about 400 MPa, as typical of SMA. It is also noticeable that the superelastic plateau may occur sooner and to higher values of strain when compared to the base material.

5.6.2 - Cycling Behavior

- Cycling Tests

The results of the cycling tests performed on the welded samples are summarized in Table 5.4 and Figures 5.13 to 5.16 present the stress-strain curves for the cycling tests with elongations of 4, 6, 8 and 12%, respect

Table 5.4 - Cycling Tests results.

Specimen Reference	Test Parameters			Obs.
	Elongation [%]	Number of cycles	Test speed [mm/min]	
# 1.4.4	4	600	2	No rupture
# 1.3.1	6			No rupture
# 1.3.3	7			No rupture
# 1.1.1	8			No rupture
# 1.2.2	12			No rupture
# 1.1.2	12			No rupture

Regardless of the chronology of the tests, the plots are presented, according to Table 5.4 from Figure 5.13 to 5.16.

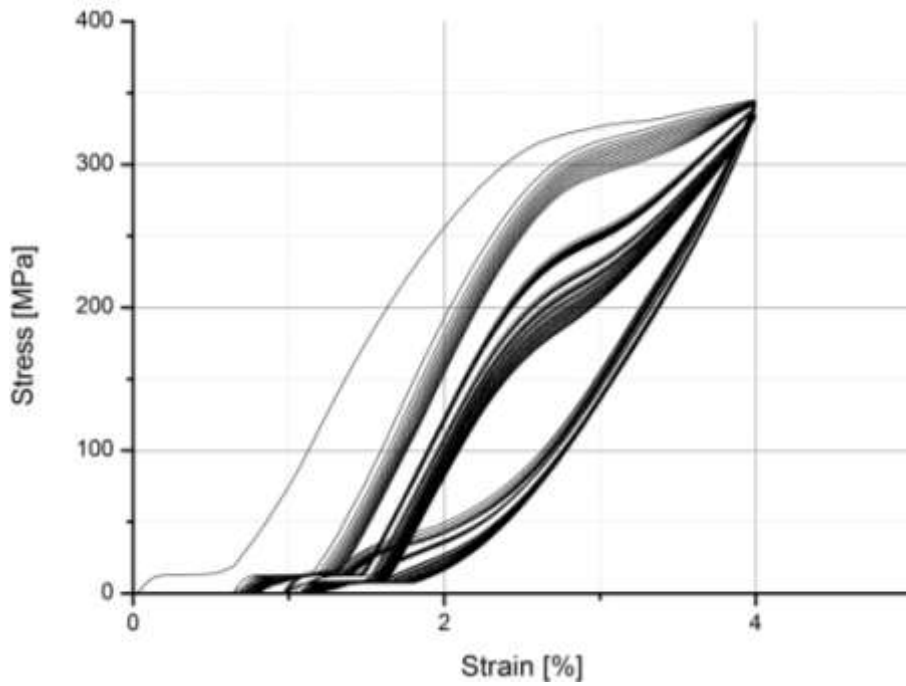


Figure 5.13 - Cycling test up to 4% elongation.

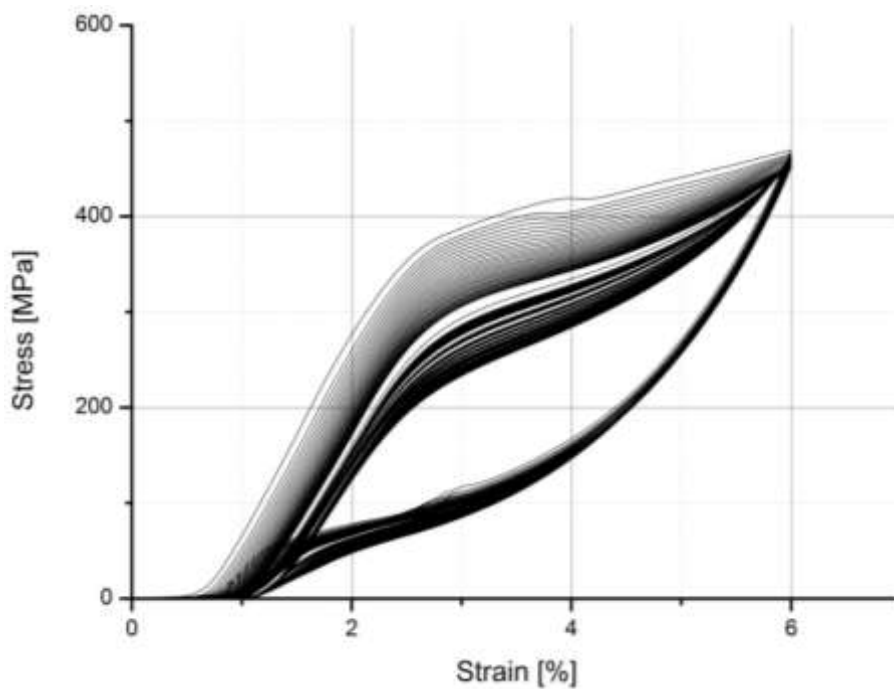


Figure 5.14 - Cycling test up to 6% elongation.

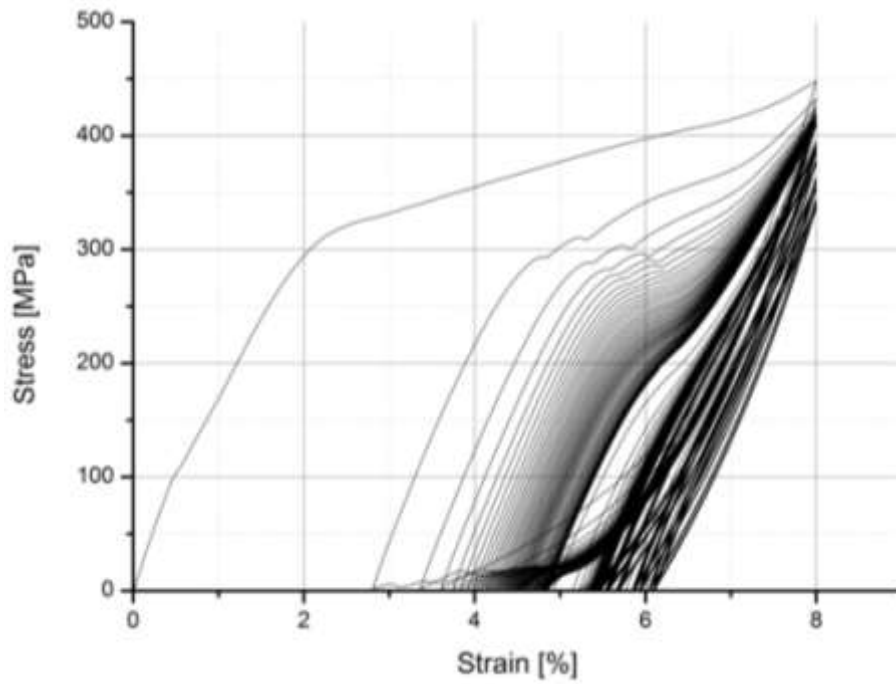


Figure 5.15 - Cycling test up to 8% elongation.

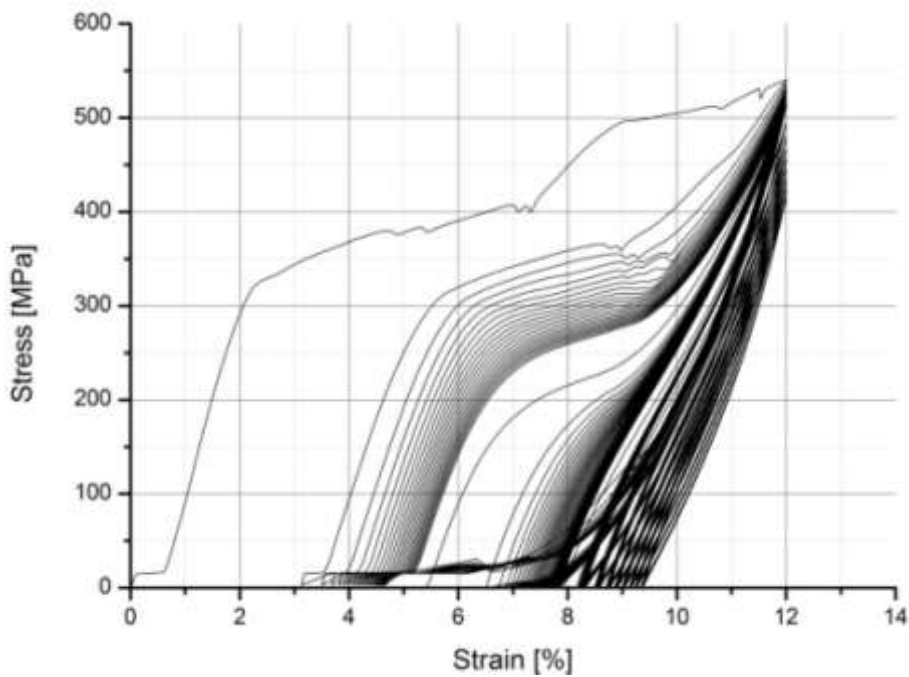


Figure 5.16 - Cycling test up to 12% elongation

Clearly, for elongations up to 6% a good behaviour is seen, while above this, sliding and irregularities were detected. Up to 8% the damping capacity is severely reduced or almost suppressed

- Accumulated Irrecoverable Strain

Analysing the evolution of the accumulated irrecoverable strain for the cycled specimens (Figures 5.17 to 5.19), it is seen that for an elongation of 4 %, the irrecoverable extension tends to a constant value of 1.2 %, which is about 30 % of the imposed elongation. That is, samples recover 70 % of induced strain. When compared to the one reported by Vieira [1] for laser welding (17 %), this is much higher, which was expected due to the fact the grain size in the fusion zone is coarser than the obtained with laser welding.

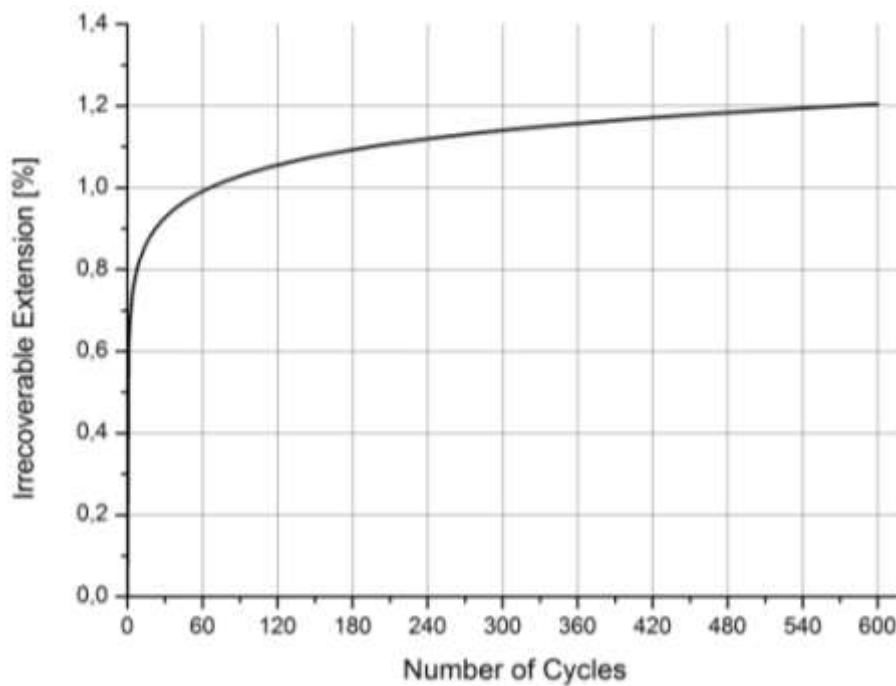


Figure 5.17- Evolution of the accumulated irrecoverable strain for specimen cycled at 4%.

For induced strain of 6% (Figure 5.18), can be noticed that irrecoverable accumulated strain of the specimen # 1.3.1 present 3 different phases. In the first, up to 150 cycles there is a rearrangement leading to the specimen to accommodate and recover some of the strain induced. In the second one, from cycle 150th to the 390th there is a stabilization in the accumulated irrecoverable strain. Afterwards, until the last cycle, the accumulated irrecoverable strain appears to increase without any indication of a possible stabilization, but at low values of strain (less than 1%).

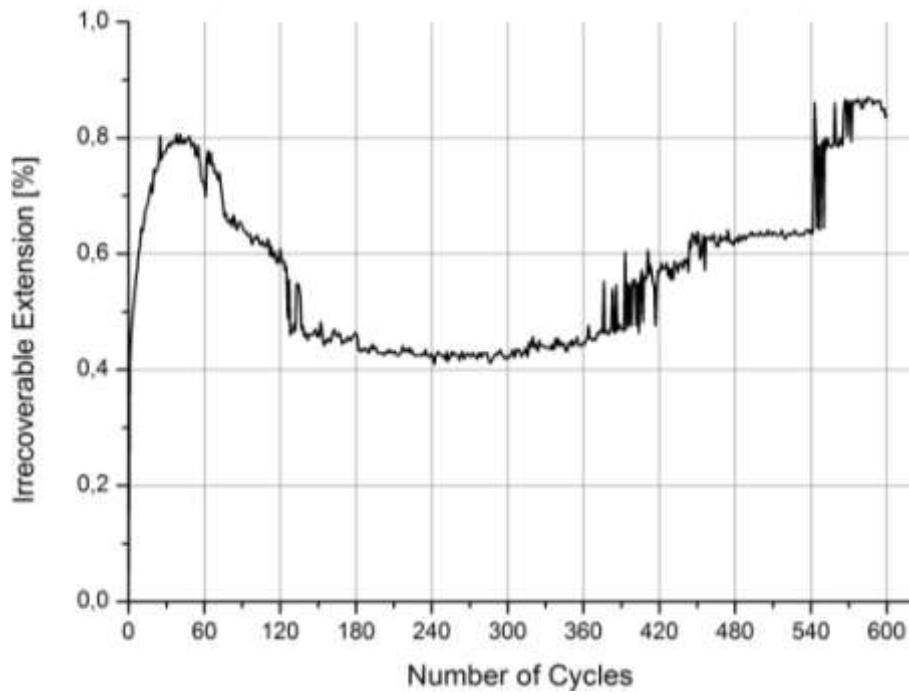


Figure 5.18 - Evolution of the accumulated irrecoverable strain for specimen cycled at 6%.

By a similar analysis and as expected from Figure 5.19 cycling at elongations of 12% result in non recoverable extensions of about 75%, that is there is a recovery of just 25%.

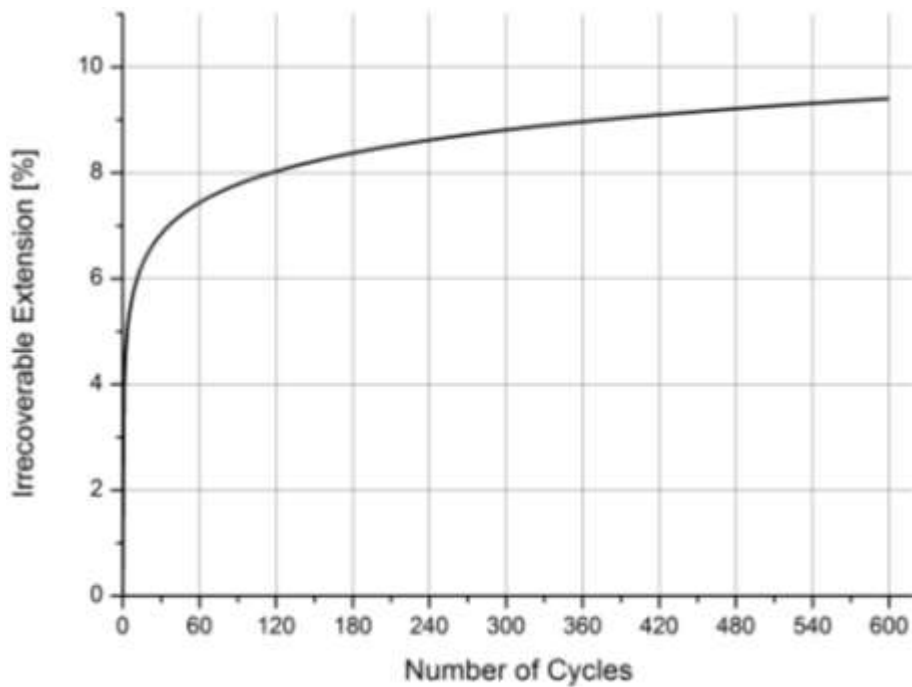


Figure 5.19 - Evolution of the accumulated irrecoverable strain for specimen cycled at 12%

5.7 - Shape Memory Effect Evaluation

The Shape Memory Effect Evaluation was performed on four distinct specimens. Three of them were previously used on the cyclic tests having a percentage of irrecoverable strain. The results are presented in Table 5.5. The variation of the irrecoverable angle (Ω) with time of the specimen, without any previous test done, is depicted in Figure 5.20.

Table 5.5- Shape Memory Effect results

Specimen Reference	Previous Cyclic Test		Induced Strain [%]	SME Evaluation		Obs.
	Elongation [%]	Irrecoverable Strain [%]		Irrecoverable Angle (Ω) [°]	Time [min.sec]	
# 1.2.1	-	-	6.7	0	3.35	FR
# 1.3.1	6.0	1.04		0	3.05	FR
# 1.1.1	8.0	6.1		0	4.00	FR

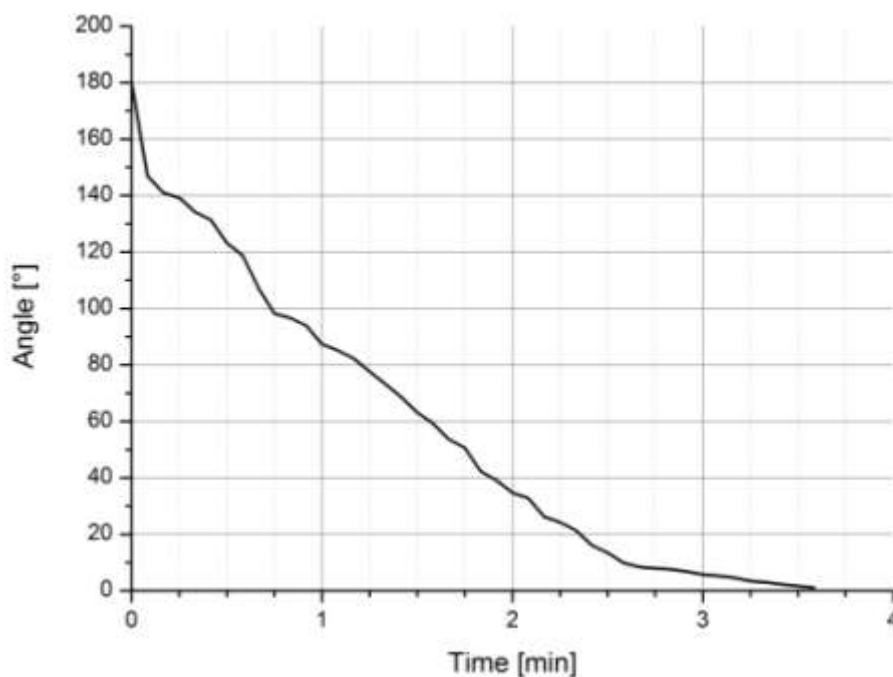


Figure 5.20 - SME evaluation of specimen #1.2.1 - Variation of the irrecoverable angle (Ω) with time.

Results summarized in Table 5.5 show that, even the specimens previously subjected to cycling tests fully recovered. With these results there is no evidence that the shape memory effect is affected by the welding procedure.

6 - CONCLUSIONS AND FURTHER WORK

Similar NiTi butt joints on 1.5 mm thick plates were produced using TIG welding process.

For this, dedicated equipment was designed and built to fix the plates during arc welding under inert gas shielding on the face and in the root.

Welds were successfully achieved without macroscopic defects, such as pores and distortions. Very superficial oxidation was seen on the top surface due to insufficient shielding gas flow on the weld face.

The welds were characterised for structural (SEM, EDS, XRD and DSC) and mechanical evaluation (tensile, cycling and SME) and from this work the following conclusions can be drawn:

- Microscopic observations, carried out on the transverse sections of the welded joints, showed an epitaxial grain growth and a narrow heat affected zone due to the low thermal coefficient of NiTi. In the centre of the weld bead Ti_2Ni phase was identified in the interdendritic boundaries. The enrichment in Ti in the fusion zone was expected since the heat input was high (1512 kJ/cm) and Ni has a vapour pressure higher than Ti. Near the interface between the HAZ and the FZ, the

cooling rate prevented the volatilization of Ni leading to the formation of $TiNi_3$. EDS analysis of the FZ confirmed a decrease in Ni atomic percentage.

- The existence of precipitates was not possible to identify by XRD eventually due to the fact that their content is below the detection limit of the available equipment. Thus, only Ni-Ti B2 phase was identified.
- SEM observations showed a regular structure free of tungsten contamination from the non-consumable electrode.
- Microhardness measurements were carried out near the top and near the weld root. Hardness variations in both profiles, are not very significant, though there is a softening of the FZ.
- DSC tests were performed in both base material and fusion zone, being possible to identify transformation temperatures during cooling and heating conditions. The two step transformation upon cooling on the BM gives place to a long and stretched transformation on the FZ. The M_s temperature varies from -45 to 5 °C in the FZ and this can be a limitation in the use of TIG in welding NiTi. The transformation from B2 structure of austenite to R-Phase, in the FZ, can be hidden in this long transformation. During heating there is also a long transformation from B19' martensite to B2 austenite in the FZ but the A_f temperature of both BM and FZ present a difference between them of 2 °C. The long transformation curve, upon heating and cooling, suggests that there is a gradient of transformation temperatures because of the chemical composition gradient along the FZ. The chemical composition gradient is due to the thermal cycle variation induced by the welding process, from the HAZ/FZ interface to the centre of the weld bead.
- The welded specimens were subjected to tensile testing up to rupture and to cycling testing for 4, 6, 8 and 12% of strain, in order to evaluate the mechanical properties of the welded sample. Results shown a significant decrease of the UTS of the welded specimens due to the increase in grain size in the FZ. Despite this, elongation to fracture remains in the same order of magnitude as the base material. A superelastic plateau still was observed at stress levels of about 400 MPa, which is still a typical value for NiTi.
- Cycling tests shown that for high values of induced strain the specimen does not have the ability to recover its initial shape. The accumulated irrecoverable strain increases as the number of cycles increase and tends to stabilize at values above 30% for strains up to 4% which is higher than observed for laser welding [1] that was of 17 %. For cycling tests above this strain the material behaviour is non consistent.

- Nevertheless, a complete recovery of initial shape was observed when testing the shape memory effect on a dedicated device that introduces a deformation of 6.7%. That is, evaluating the Shape Memory Effect there is no evidence that this property was affected by the welding procedure. Even specimens previously subjected to cyclic tests, fully recovered their initial shape.

REFERENCES

- [1] L. M. A. Vieira, *“Laser welding of shape memory alloys”*, MSc Thesis on Mechanical Engineering presented at Faculdade de Ciência e Tecnologia, Universidade Nova de Lisboa, 2010.
- [2] Otsuka, K.; Wayman, C. M. – *Shape Memory Materials*. Cambridge University Press. Cambridge 1998.
- [3] Miranda, R. M. et al. – *Shape Memory Alloys: Exiting and Emerging Applications*. Advances in Materials Science Research. ISBN: 978-1-61209-116-7. Vol. 6, pp. 241-265, 2011.
- [4] Marjan Bahraminasab and Barkawi Bin Sahari (2013). NiTi Shape Memory Alloys, Promising Materials in Orthopedic Applications, Shape Memory Alloys - Processing, Characterization and Applications, Dr. Francisco Manuel Braz Fernandes (Ed.), ISBN: 978-953-51-1084-2, InTech, DOI: 10.5772/48419. Available from: <http://www.intechopen.com/books/shape-memory-alloys-processing-characterization-and-applications/niti-shape-memory-alloys-promising-materials-in-orthopedic-applications>

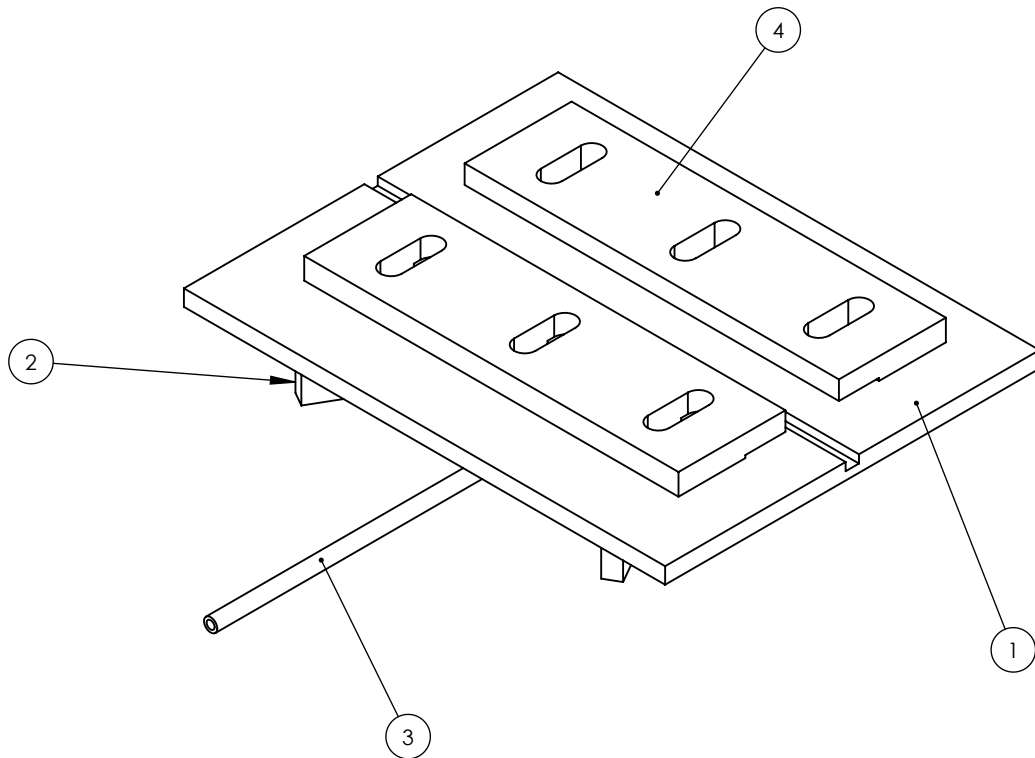
- [5] Shaw J.A. - "A thermomechanical model for a 1-D shape memory alloy wire with propagating instabilities". Intern. J. of Solids and Structures, 39 (2002) p.1275-1305.
- [6] J. P. S. Oliveira, "Correlation between the Mechanical Cycling Behavior and Microstructure in Laser Welded Joints Using NiTi Memory Shape Alloys", MSc Thesis on Mechanical Engineering presented at Faculdade de Ciência e Tecnologia, Universidade Nova de Lisboa, 2012.
- [7] Otsuka, K.; Ren, X., "Physical metallurgy of Ti-Ni base Shape Memory Alloys," *Progress in Materials Science*, 50, 511-678, 2005.
- [8] D. C. Lagoudas, "Shape Memory Alloys: Modeling and Engineering Applications." Springer, 2008.
- [9] Morgan, N.B.; Broadley, M., "Taking the art out of smart! - Forming processes and durability issues for the application of NiTi shape memory alloys in medical devices," in *Materials & Processes for Medical Devices Conference*, Anaheim, California (2004) pp. 247-252.
- [10] Ekahinia Mohammad H.; Hashemi Mahdi; Tabesh Majid; Bhaduri Sari B. - "Manufacturing and processing of NiTi implants: A review." *Progress in Materials Science* 57 (2012) pp. 911-946.
- [11] K. Weinert, V. Petzoldt; "Machining of NiTi based shape memory alloys"; *Materials Science & Engineering A* 378 (2004) pp.180-184.
- [12] Pires, J. Norberto; Loureiro, Altino; Bölmsjö, Gunnar; "Welding Robots - Technology, System Issues and Application"; Springer, Portugal, 2006.
- [13] Santos, J. F.; Quintino, L; "Processos de Soldadura"; 2ª Edição; Edições Técnicas do Instituto de Soldadura e Qualidade, Portugal.
- [14] W. M. Steen;" *Laser Material Processing*"; Springer, 2010."
- [15] Assunção, E.; Williams S.; "Comparison of continuous wave and pulsed wave laser welding effects"; *Optics and Laser in Engineering*, 51, 6 (2013) pp. 674-680.

-
- [16] Ikai, A.; Kimura, K.; Tobushi, H., "*TIG Welding and Shape Memory Effect of TiNi Shape Memory Alloy*," *Journal of intelligent Material Systems and Structures*, 7, 6 (1996), 646-655.
- [17] Ming H. Wu and L. McD. Schetky; "Industrial Applications for Shape memory alloys"; *Proceedings for the International Conference on Shape Memory Superelastic Technologies*, Pacific Grove, California, P.171-182, 2000.
- [18] C. L. F. Guerreiro, "*Avaliação de emissões de nanopartículas resultantes de processos de soldadura por fusão em aços*", MSc Thesis on Mechanical Engineering presented at Faculdade de Ciência e Tecnologia da Universidade Nova de Lisboa, 2012.
- [19] "*Nitinol Technical Properties*" [Online]. Available: <http://jmmedical.com/resources/221/Nitinol-Technical-Properties.html>.
- [20] TELWIN - Welding Technologies. (2014, September) TELWIN, TECHNOLOGY TIG 182 AC/DC-HF/LIFT [Online]. Available: "<http://www.telwin.com/webtelwin/site.nsf/webapridocumento?openform&E|3||852030|81>"
- [21] "PerkinElmer - Differential Scanning Calorimetry" [Online]. Available http://www.perkinelmer.com/CMSResources/Images/44-74542GDE_DSCBeginnersGuide.pdf
- [22] Beer, Ferdinand P.; Johnston, E. Russel Jr.; DeWolf, John T.; *Mechanics of Materials*, 4th ed.: The McGraw-Hill Companies, Inc, 2006.
- [23] E. A. Brandes and G. B. Brook, Eds., "*Smithells Metals Reference Book*", 7th ed. Butterworth-Heinemann, 1998.

ANNEXES

A - Positioning Device Technical Drawings

The technical drawings of the fixture system and chamber used for TIG welding are now presented. The system was built in DEMI section of Industrial Technology.



1	Base			1			
2	Foot			2			
1	Feeding Tube			3			
2	Position Ruler			4			
Nº	DESIGNAÇÃO	Nº DA NORMA Nº DESENHO	MATERIAL	Nº REF	PRODUTO SEMI-ACABADO Nº MOLDE Nº MATRIZ	PESO	OBSERVAÇÕES

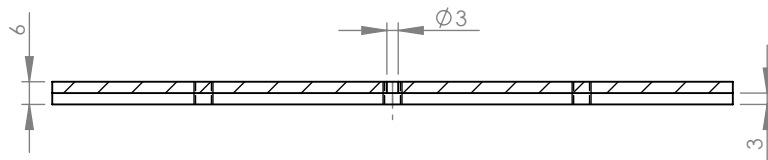
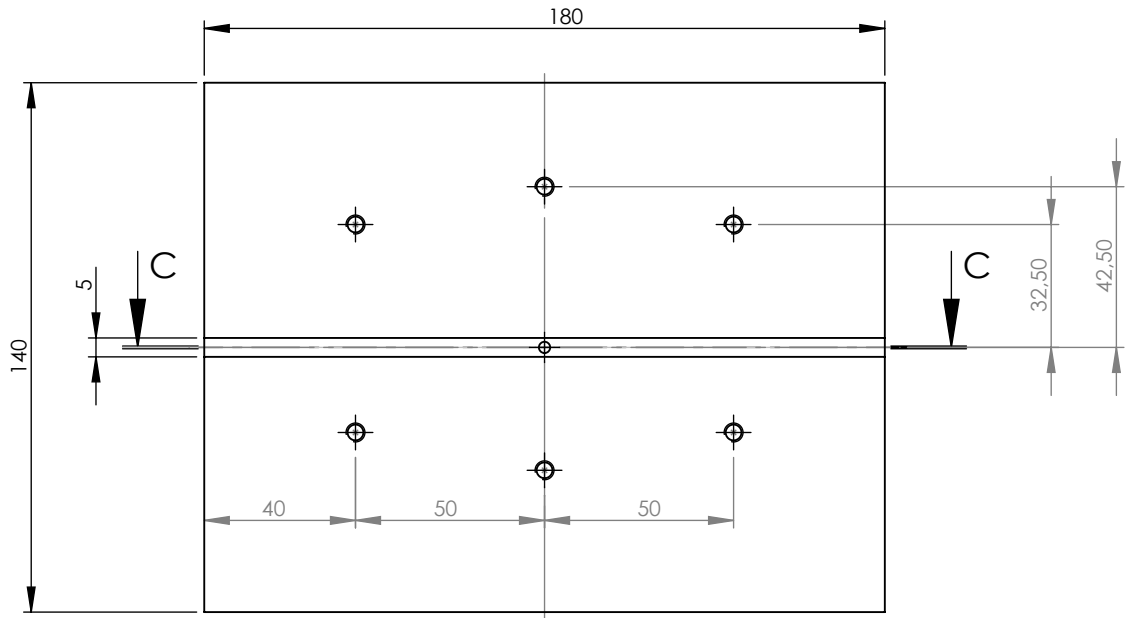
David B. 20/09/14

FIXTURE SYSTEM
TIG WELDING of SMAs

UNL-FCT

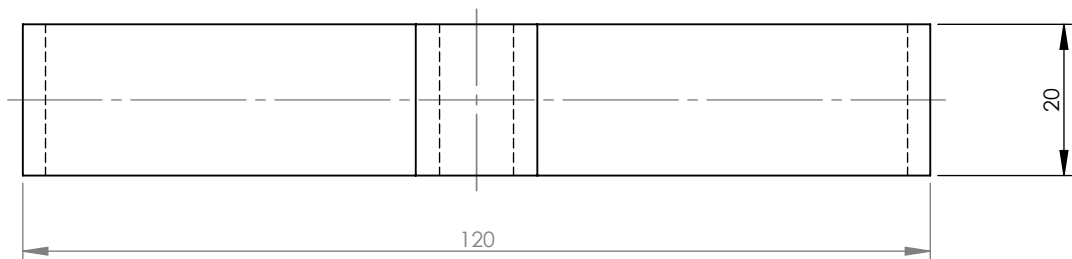
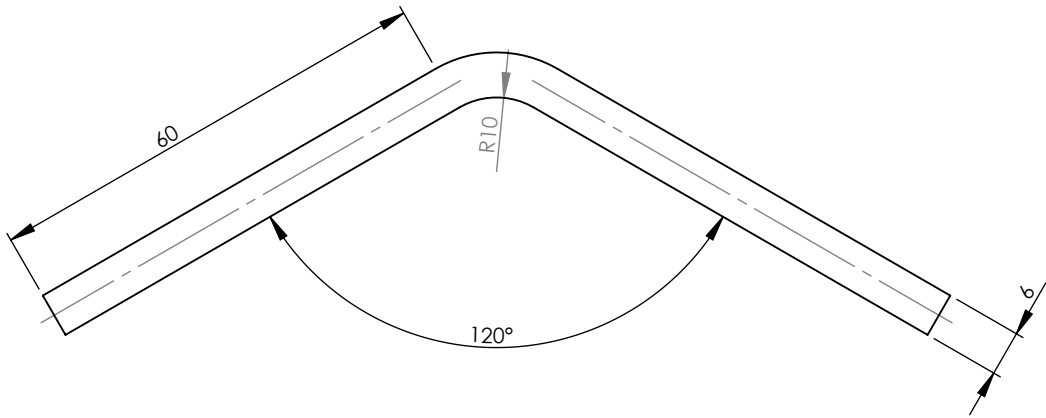
Scale
1:2

POSITION SYSTEM

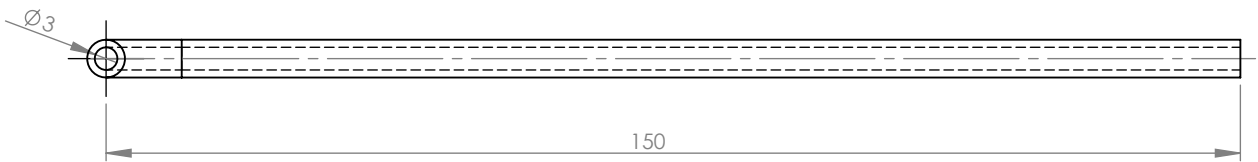
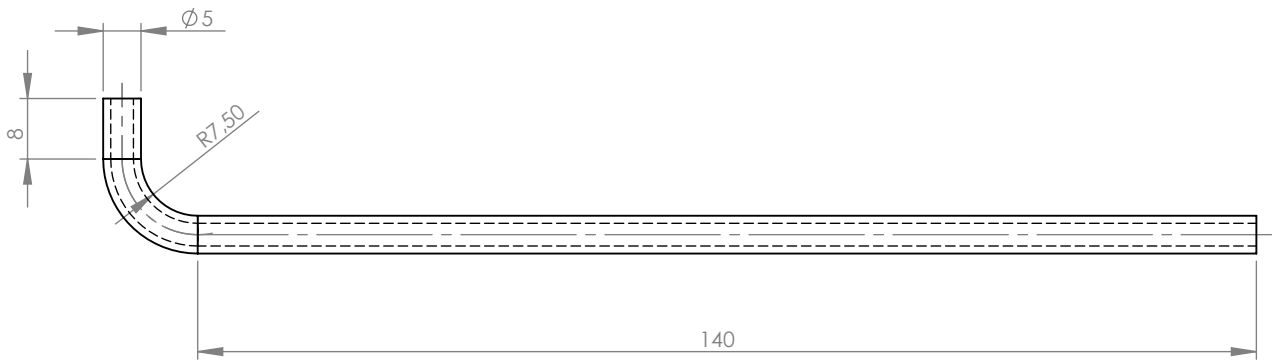


SECTION C-C

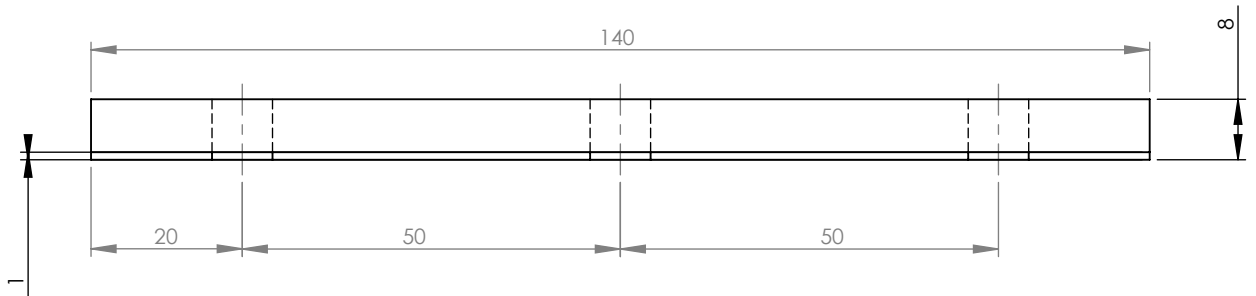
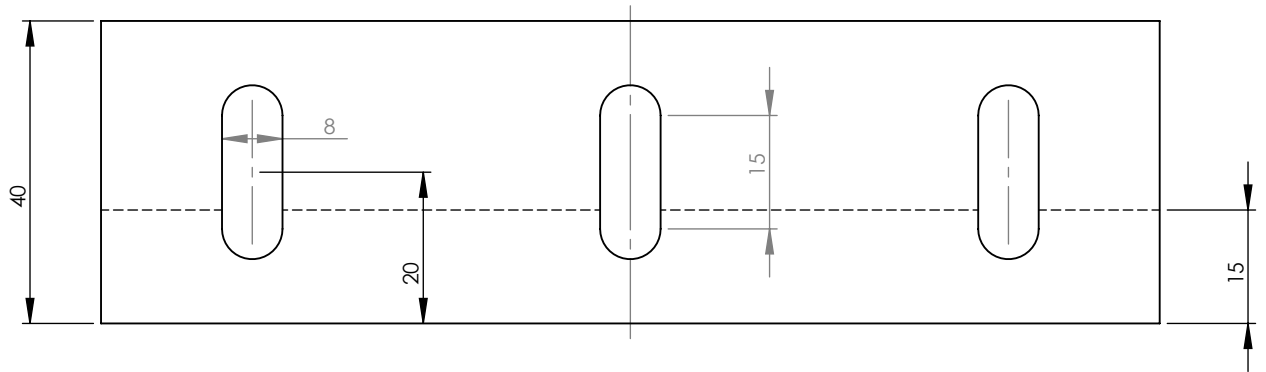
David B. 20/09/14			UNL-FCT	
			FIXTURE SYSTEM TIG WELDING of SMAs	
Scale 1:2			BASE	



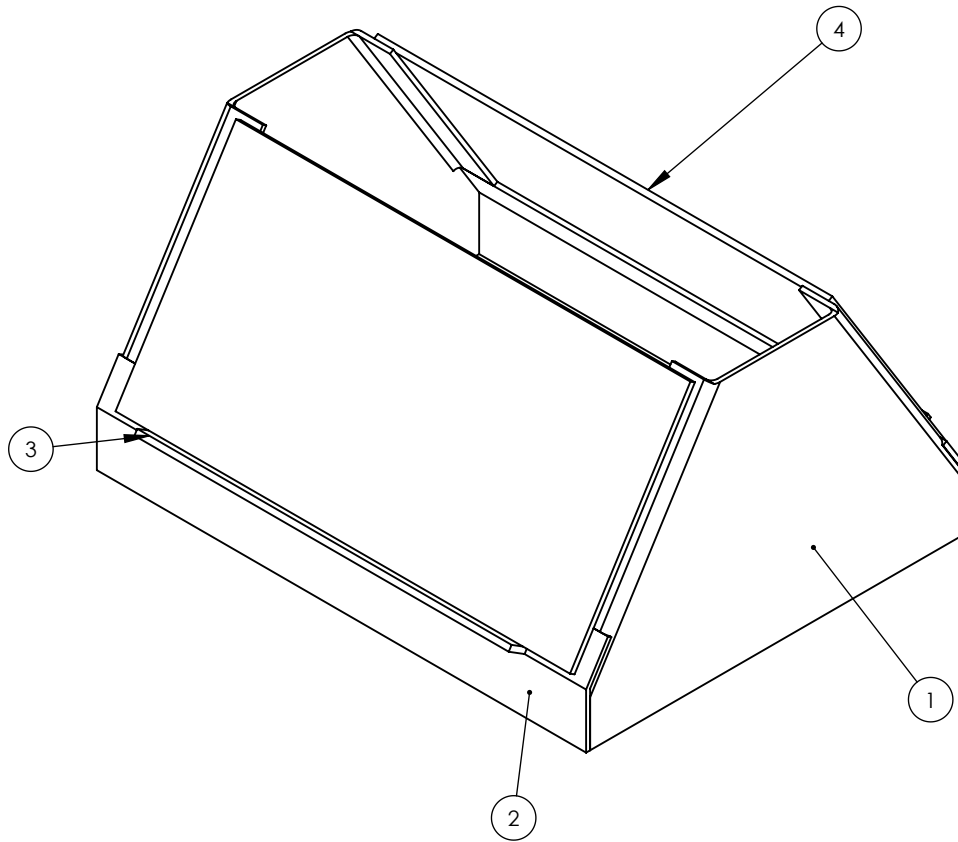
David B. 20/09/14			UNL-FCT																					
			FIXTURE SYSTEM TIG WELDING of SMAs																					
Scale 1:1			FOOT																					
			<table border="1"> <tr> <td></td><td></td><td></td><td></td><td></td><td></td><td></td><td></td><td></td><td></td> </tr> <tr> <td></td><td></td><td></td><td></td><td></td><td></td><td></td><td></td><td></td><td></td> </tr> </table>																					



David B. 20/09/14			UNL-FCT	
			FIXTURE SYSTEM TIG WELDING of SMAs	
Scale 1:1			FEEDING TUBE	



David B. 20/09/14			UNL-FCT																					
			FIXTURE SYSTEM TIG WELDING of SMAs																					
Scale 1:1			POSITION RULER																					
			<table border="1"> <tr> <td></td><td></td><td></td><td></td><td></td><td></td><td></td><td></td><td></td><td></td> </tr> <tr> <td></td><td></td><td></td><td></td><td></td><td></td><td></td><td></td><td></td><td></td> </tr> </table>																					



2	Lateral Panel			1			
2	Frontal Panel			2			
2	Acrylic Panel Support			3			
2	Acrylic Panel			4			
Nº	DESIGNAÇÃO	Nº DA NORMA Nº DESENHO	MATERIAL	Nº REF	PRODUTO SEMI-ACABADO Nº MOLDE Nº MATRIZ	PESO	OBSERVAÇÕES

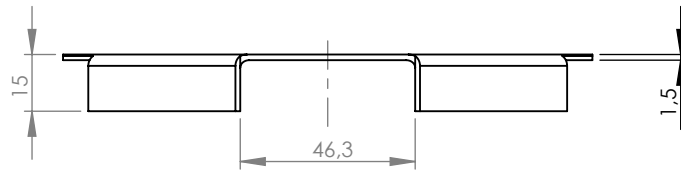
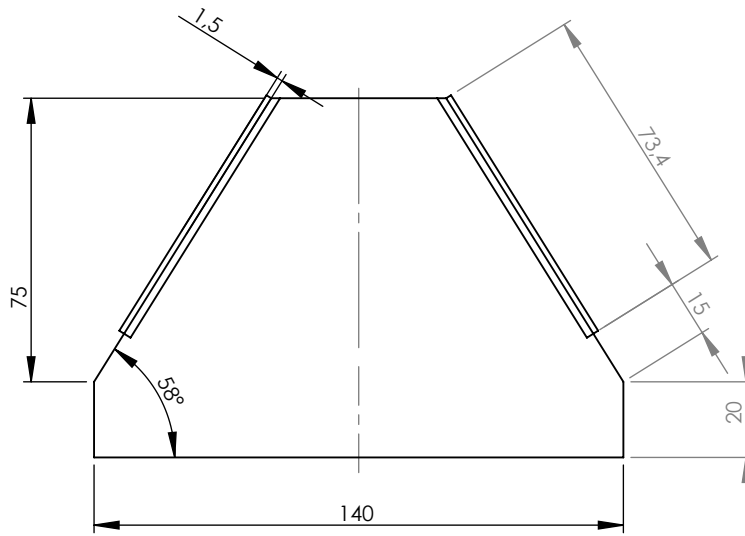
David B. 20/09/14

FIXTURE SYSTEM
TIG WELDING of SMAs

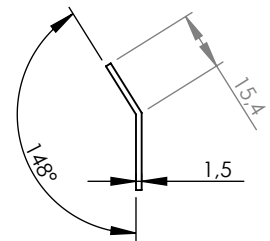
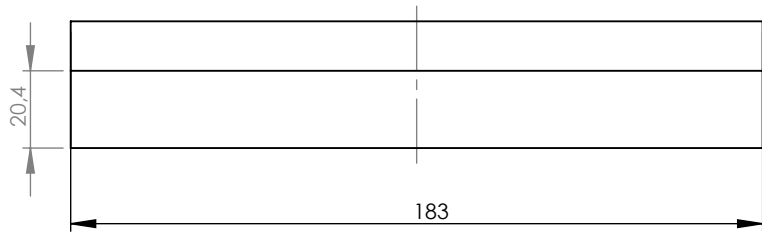
UNL-FCT

Scale
1:2

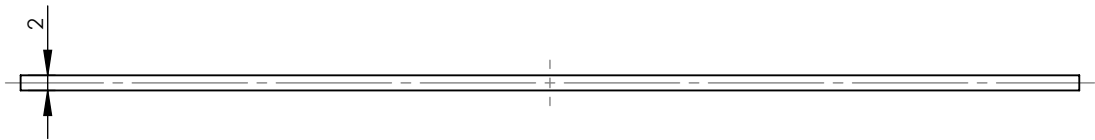
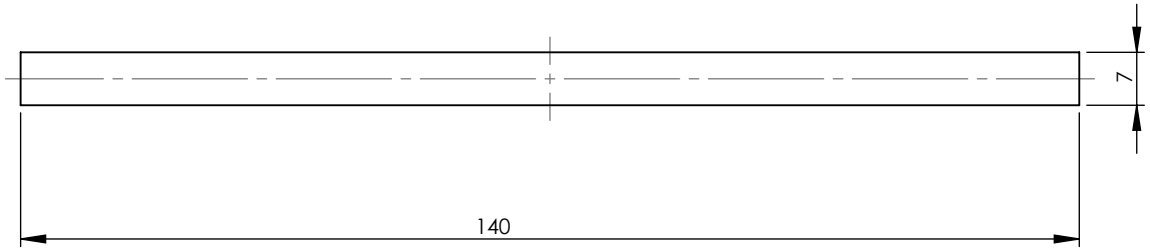
CHAMBER



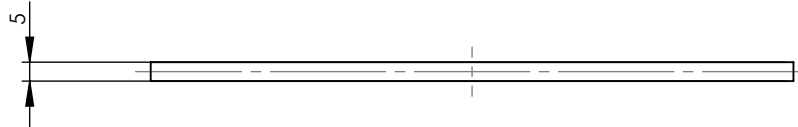
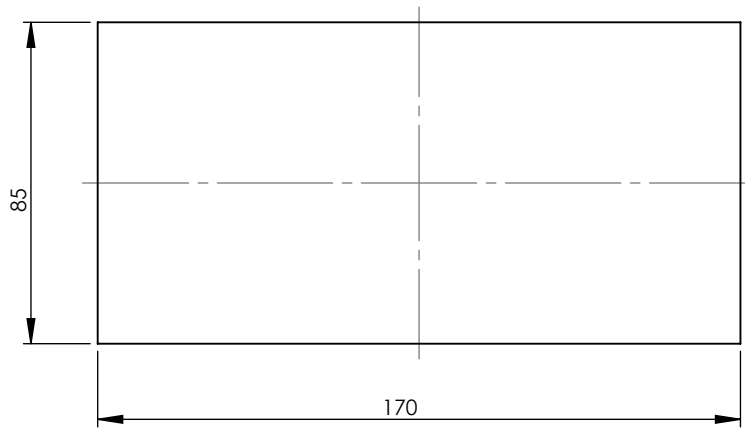
David B. 20/09/14			UNL-FCT																					
			FIXTURE SYSTEM TIG WELDING of SMAs																					
Scale 1:2			LATERAL PANEL																					
			<table border="1"> <tr> <td></td><td></td><td></td><td></td><td></td><td></td><td></td><td></td><td></td><td></td> </tr> <tr> <td></td><td></td><td></td><td></td><td></td><td></td><td></td><td></td><td></td><td></td> </tr> </table>																					



David B. 20/09/14			UNL-FCT																					
			FIXTURE SYSTEM TIG WELDING of SMAs																					
Scale 1:2			FRONT PANEL																					
			<table border="1"> <tr> <td></td><td></td><td></td><td></td><td></td><td></td><td></td><td></td><td></td><td></td> </tr> <tr> <td></td><td></td><td></td><td></td><td></td><td></td><td></td><td></td><td></td><td></td> </tr> </table>																					



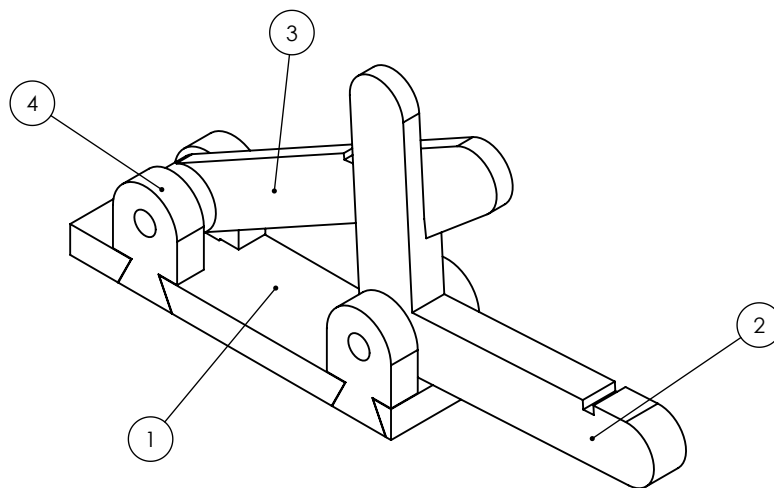
David B. 20/09/14			FIXTURE SYSTEM TIG WELDING of SMAs	UNL-FCT																				
Scale 1:1																								
ACRYLIC SUPPORT			<table border="1"> <tr> <td></td><td></td><td></td><td></td><td></td><td></td><td></td><td></td><td></td><td></td> </tr> <tr> <td></td><td></td><td></td><td></td><td></td><td></td><td></td><td></td><td></td><td></td> </tr> </table>																					



David B. 20/09/14			UNL-FCT																					
			FIXTURE SYSTEM TIG WELDING of SMAs																					
Scale 1:2			ACRYLIC PANEL																					
			<table border="1"> <tr> <td></td><td></td><td></td><td></td><td></td><td></td><td></td><td></td><td></td><td></td> </tr> <tr> <td></td><td></td><td></td><td></td><td></td><td></td><td></td><td></td><td></td><td></td> </tr> </table>																					

B - Trigger Device Technical Drawings

The technical drawings of the trigger device used for activating the TIG torch are now presented. The system was built using 3D printing technology.



1	Base			1			
1	Activator			2			
1	Holder			3			
4	Lateral Support			4			
Nº	DESIGNAÇÃO	Nº DA NORMA Nº DESENHO	MATERIAL	Nº REF	PRODUTO SEMI-ACABADO Nº MOLDE Nº MATRIZ	PESO	OBSERVAÇÕES

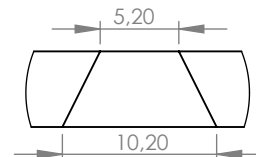
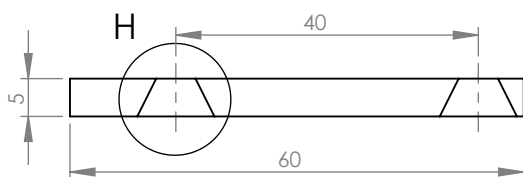
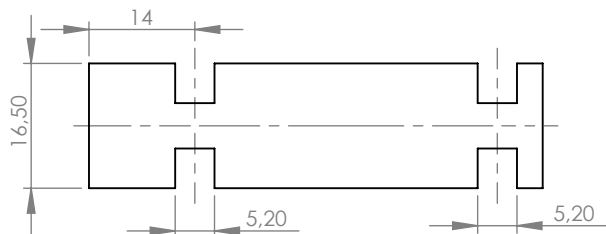
David B. 20/09/14

TRIGGER DEVICE
TIG WELDING of SMAs

UNL-FCT

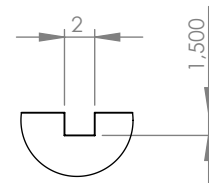
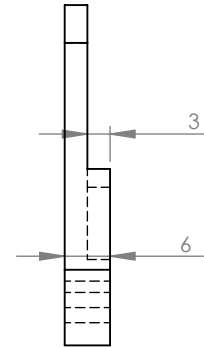
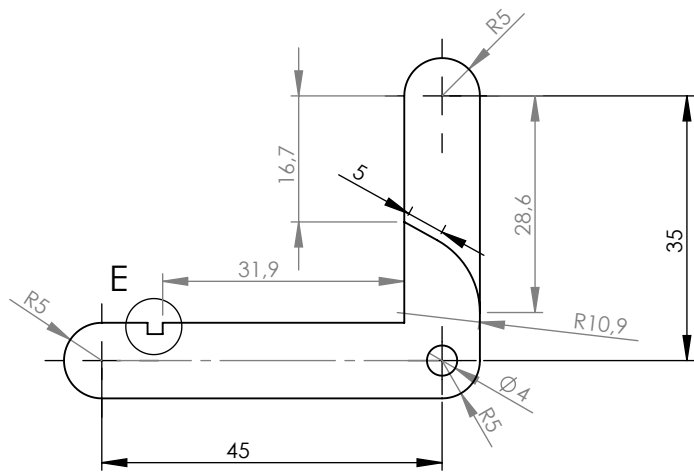
Scale
1:1

TRIGGER DEVICE

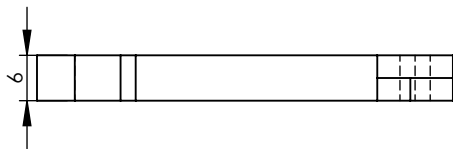


DETAIL H
SCALE 2 : 1

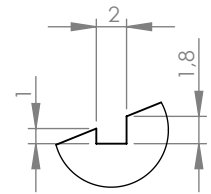
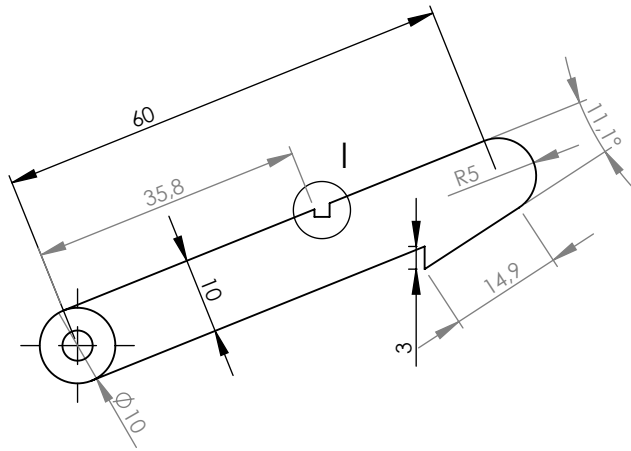
David B. 20/09/14			TRIGGER DEVICE TIG WELDING of SMAs	
Scale 1:1			UNL-FCT	
BASE				



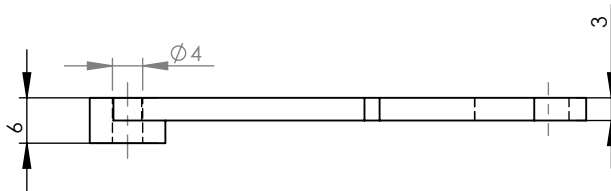
DETAIL E
SCALE 2 : 1



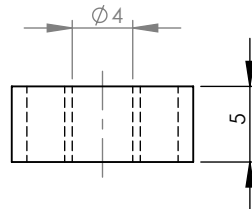
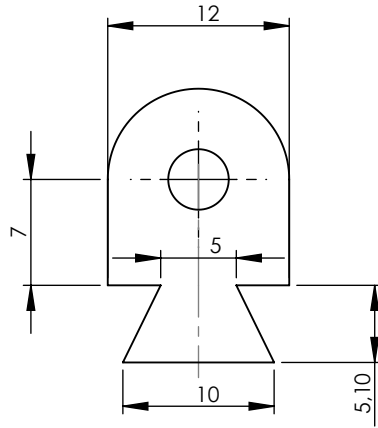
David B. 20/09/14			TRIGGER DEVICE TIG WELDING of SMAs	
Scale 1:1			UNL-FCT	
ACTIVATOR				



DETAIL I
SCALE 2 : 1



David B. 20/09/14			UNL-FCT	
			TRIGGER DEVICE TIG WELDING of SMAs	
Scale 1:1			HOLDER	



David B. 20/09/14			UNL-FCT	
			TRIGGER DEVICE TIG WELDING of SMAs	
Scale 2:1			LATERAL SUPPORT	

